

ReQFlow: Rectified Quaternion Flow for Efficient and High-Quality Protein Backbone Generation

Angxiao Yue¹ Zichong Wang² Hongteng Xu^{1,3*}

¹Gaoling School of Artificial Intelligence, Renmin University of China

²School of Statistics, Renmin University of China

³Beijing Key Laboratory of Big Data Management and Analysis Methods

hongtengxu@ruc.edu.cn

February 21, 2025

Abstract

Protein backbone generation plays a central role in *de novo* protein design and is significant for many biological and medical applications. Although diffusion and flow-based generative models provide potential solutions to this challenging task, they often generate proteins with undesired designability and suffer computational inefficiency. In this study, we propose a novel rectified quaternion flow (ReQFlow) matching method for fast and high-quality protein backbone generation. In particular, our method generates a local translation and a 3D rotation from random noise for each residue in a protein chain, which represents each 3D rotation as a unit quaternion and constructs its flow by spherical linear interpolation (SLERP) in an exponential format. We train the model by quaternion flow (QFlow) matching with guaranteed numerical stability and rectify the QFlow model to accelerate its inference and improve the designability of generated protein backbones, leading to the proposed ReQFlow model. Experiments show that ReQFlow achieves state-of-the-art performance in protein backbone generation while requiring much fewer sampling steps and significantly less inference time (e.g., being $37\times$ faster than RFDiffusion and $62\times$ faster than Genie2 when generating a backbone of length 300), demonstrating its effectiveness and efficiency. The code is available at <https://github.com/AngxiaoYue/ReQFlow>.

1 Introduction

De novo protein design [12, 19] aims to design rational proteins from scratch with specific properties or functions, which has many biological and medical applications, such as developing novel enzymes for biocatalysis [15] and discovering new drugs for diseases [29, 27]. This task is challenging due to the extremely huge design space of proteins. For simplifying the task, the mainstream *de novo* protein design strategy takes protein backbone generation (i.e., generating 3D protein structures without side chains) as the key step that largely determines the rationality and basic properties of designed proteins.

Focusing on protein backbone generation, many deep generative models, especially those diffusion and flow-based models [10, 32, 20, 35, 34, 2, 11, 22], have been proposed as potential solutions. However, these models often generate protein backbones with poor designability (the key metric indicating the quality of generated protein backbones), especially for proteins with long residue chains.

*Hongteng Xu is the corresponding author of this work.

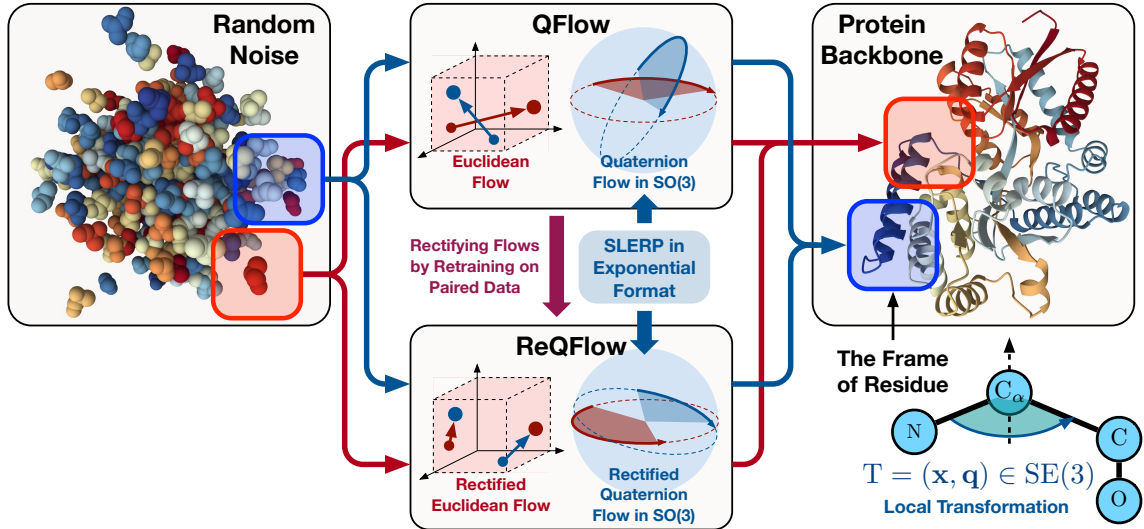


Figure 1: An illustration of our rectified quaternion flow matching method, in which each residue is represented as a frame associated with a local transformation.

In addition, diffusion or flow models often require many sampling steps to generate protein backbones, resulting in high computational complexity and long inference time. As a result, the above drawbacks on generation quality and computational efficiency limit these models in practical large-scale applications.

To overcome the above challenges, we propose a novel rectified quaternion flow (ReQFlow) matching method, achieving fast and high-quality protein backbone generation. As illustrated in Figure 1, our method learns a model to generate a local 3D translation and a 3D rotation respectively from random noise for each residue in a protein chain. Different from existing models, the proposed model represents each rotation as a unit quaternion and constructs its quaternion flow in $SO(3)$ by spherical linear interpolation (SLERP) in an exponential format [28], which can be learned by our quaternion flow (QFlow) matching strategy. Furthermore, given a trained QFlow model, we leverage the rectified flow technique in [23], re-training the model based on the paired noise and protein backbones generated by the model itself. The rectified QFlow (i.e., ReQFlow) model leads to non-crossing sampling paths in \mathbb{R}^3 and $SO(3)$, respectively, when generating translations and rotations. As a result, we can apply fewer sampling steps to accelerate the generation process significantly.

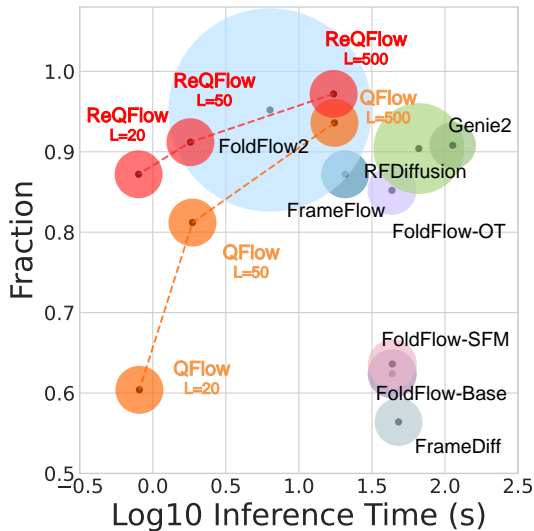


Figure 2: Comparisons for each method. For each model, the size of its circle indicates the model size, and the location of the circle’s centroid indicates the logarithm of the average inference time when generating a protein backbone with length $N = 300$ and the Fraction score of designable protein backbones. For QFlow and ReQFlow, we set the sampling step $L \in \{20, 50, 500\}$, respectively.

We demonstrate the rationality and effectiveness of ReQFlow compared to existing diffusion and flow-based methods. In particular, thanks to the exponential format SLERP, ReQFlow is learned and implemented with guaranteed numerical stability and computational efficiency, especially when the rotation angle is close to 0 or π . Experimental results demonstrate that ReQFlow achieves state-of-the-art performance, generating high-quality protein backbones with significantly reduced inference time. Furthermore, ReQFlow consistently maintains effectiveness and efficiency in generating long-chain protein backbones (e.g., the protein backbones with over 500 residues), where all baseline models suffer severe performance degradation. As shown in Figure 2, ReQFlow outperforms existing methods and generates high-quality protein backbones, whose designability Fraction score is 0.972 when sampling 500 steps and 0.912 when merely sampling 50 steps.

2 Related Work and Preliminaries

2.1 Protein Backbone Generation

Many diffusion and flow-based methods have been proposed to generate protein backbones. These methods often parameterize protein backbones like AlphaFold2 [13] does, representing each protein’s residues as a set of SE(3) frames. Accordingly, FrameDiff [35] generates protein backbones by two independent diffusion processes, generating the corresponding frames’ local translations and rotations, respectively. Following the same framework, flow-based methods like FrameFlow [34] and FoldFlow [2] replace the stochastic diffusion processes with deterministic flows.

For the above methods, many efforts have been made to modify their model architectures and improve data representations, e.g., the Clifford frame attention module in GAFL [31] and the asymmetric protein representation module in Genie [19] and Genie2 [20]. In addition, some methods leverage large-scale pre-trained models to improve generation quality. For example, RFDiffusion [32] utilizes the pre-trained RoseTTAFold [1] as the backbone model. FoldFlow2 [11] improves FoldFlow by using a protein large language model for residue sequence encoding.

Currently, the above methods often suffer the conflict on computational efficiency and generation quality. The state-of-the-art methods like RFDiffusion [32] and Genie2 [20] need long inference time to generate protein backbones with reasonable quality. FrameFlow [34] and GAFL [31] significantly improves inference speed while lags behind RFDiffusion and Genie2 in protein backbone quality. Moreover, all the methods suffer severe performance degradation when generating long-chain protein backbones. These limitations motivate us to develop the proposed ReQFlow, improving the current flow-based methods and generating protein backbones efficiently with satisfactory designability.

2.2 Quaternion Algebra and Its Applications

The proposed ReQFlow is designed based on quaternion algebra [5, 39]. Mathematically, quaternion is an extension of complex numbers into four-dimensional space, consists of one real component and three orthogonal imaginary components. A quaternion is formally expressed as $q = s + xi + yj + zk \in \mathbb{H}$, where \mathbb{H} denotes the quaternion domain, and $s, x, y, z \in \mathbb{R}$. The imaginary components $\{i, j, k\}$ satisfy $i^2 = j^2 = k^2 = ijk = -1$. Each $q \in \mathbb{H}$ can be equivalently represented as a vector $\mathbf{q} = [s, \mathbf{u}^\top]^\top \in \mathbb{R}^4$, where $\mathbf{u}^\top = [x, y, z]^\top$. Given $\mathbf{q}_1 = [s_1, \mathbf{u}_1^\top]^\top$ and $\mathbf{q}_2 = [s_2, \mathbf{u}_2^\top]^\top$, their multiplication is achieved by Hamilton product, i.e.,

$$\mathbf{q}_1 \otimes \mathbf{q}_2 = \begin{bmatrix} s_1 s_2 - \mathbf{u}_1^\top \mathbf{u}_2 \\ s_1 \mathbf{u}_2 + s_2 \mathbf{u}_1 + \mathbf{u}_1 \times \mathbf{u}_2 \end{bmatrix}, \tag{1}$$

where \times denotes the cross product.

Quaternion is a powerful tool to describe 3D rotations. For a 3D rotation in the axis-angle formulation, i.e., $\boldsymbol{\omega} = \phi \mathbf{u} \in \mathbb{R}^3$, where the unit vector \mathbf{u} and the scalar ϕ denote the rotation axis and angle, respectively, we can convert it to a unit quaternion by an exponential map [28]:

$$\mathbf{q} = \exp\left(\frac{1}{2}\boldsymbol{\omega}\right) = \left[\cos\frac{\phi}{2}, \sin\frac{\phi}{2}\mathbf{u}^\top\right]^\top \in \mathbb{S}^3, \quad (2)$$

where $\mathbb{S}^3 = \{\mathbf{q} \in \mathbb{R}^4 \mid \|\mathbf{q}\|_2 = 1\}$ is the 4D hypersphere. The conversion from a unit quaternion to an angle-axis representation is achieved by a logarithmic map:

$$\boldsymbol{\omega} = 2 \log(\mathbf{q}). \quad (3)$$

Suppose that we rotate a point $\mathbf{v}_1 \in \mathbb{R}^3$ to \mathbf{v}_2 by $\boldsymbol{\omega}$, we can equivalently implement the operation by

$$\mathbf{v}_2 = \text{Im}(\mathbf{q} \otimes [0, \mathbf{v}_1^\top]^\top \otimes \mathbf{q}^{-1}), \quad (4)$$

where $\mathbf{q}^{-1} = [\cos\frac{\phi}{2}, -\sin\frac{\phi}{2}\mathbf{u}^\top]^\top$ is the inverse of \mathbf{q} and “Im(\cdot)” denotes the imaginary components of a quaternion (i.e., the last three elements of the corresponding 4D vector). The quaternion-based rotation representation in Eq. 4 offers several advantages, including compactness, computational efficiency, and avoidance of gimbal lock [9], which has been widely used in skeletal animation [26], robotics [24], and virtual reality [17].

Besides computer graphics, some quaternion-based machine learning models have been proposed for other tasks, e.g., image processing [33, 39] and structured data (e.g., graphs and point clouds) analysis [37, 38]. Recently, some quaternion-based models have been developed for scientific problems, e.g., the quaternion message passing [36] for molecular conformation representation and the quaternion generative models for molecule generation [16, 8]. However, the computational quaternion techniques are seldom considered in protein-related tasks. Our work fill this blank, demonstrating the usefulness of quaternion algebra in protein backbone generation.

3 Proposed Method

3.1 Protein Backbone Parameterization

We parameterize the protein backbone following [13, 35, 34, 2]. As illustrated in Figure 1, each residue is represented as a frame, where the frame encodes a rigid transformation starting from the idealized coordinates of four heavy atoms: $[\text{N}^*, \text{C}_\alpha^*, \text{C}^*, \text{O}^*] \in \mathbb{R}^{3 \times 4}$. In this representation, $\text{C}_\alpha^* = [0, 0, 0]^\top$ is placed at the origin, and the transformation incorporates experimental bond angles and lengths [7]. We can derive each residue’s frame by

$$[\text{N}^i, \text{C}_\alpha^i, \text{C}^i, \text{O}^i] = \text{T}^i \circ [\text{N}^*, \text{C}_\alpha^*, \text{C}^*, \text{O}^*], \quad (5)$$

where $\text{T}^i \in \text{SE}(3)$ is the local orientation-preserving rigid transformation mapping the idealized frame to the frame of the i -th residue. In this study, we represent $\text{T}^i = (\mathbf{x}^i, \mathbf{q}^i)$, where $\mathbf{x}^i \in \mathbb{R}^3$ represents the 3D translation and a unit quaternion $\mathbf{q}^i \in \mathbb{S}^3$, which double-covers $\text{SO}(3)$, represents a 3D rotation. According to Eq. 4, the action of T^i on a coordinate $\mathbf{v} \in \mathbb{R}^3$ can be implemented as

$$\text{T}^i \circ \mathbf{v} = \mathbf{x}^i + \text{Im}(\mathbf{q} \otimes [0, \mathbf{v}^\top]^\top \otimes \mathbf{q}^{-1}). \quad (6)$$

Note that, for protein backbone generation, we can use the planar geometry of backbone to impute the coordinate of the oxygen atom O^i [34, 32], so we do not need to parameterize the rotation angle

of the bond “C $_{\alpha}$ – C”. As a result, for a protein backbone with N residues, we have a collection of N frames, resulting in the parametrization set $\Theta = \{\mathbf{T}^i\}_{i=1}^N$. Therefore, we can formulate the protein backbone generation problem as modeling and generating $\{\mathbf{T}^i\}_{i=1}^N$ automatically.

3.2 Quaternion Flow Matching

We decouple the translation and rotation of each frame, establishing two independent flows in \mathbb{R}^3 and $\text{SO}(3)$, respectively. Without the loss of generality, we define these two flows in the time interval $[0, 1]$. When $t = 0$, we sample the starting points of the flows as random noise, i.e., $\mathbf{T}_0 = (\mathbf{x}_0, \mathbf{q}_0) \sim \mathcal{T}_0 \times \mathcal{Q}_0$, where $\mathcal{T}_0 = \mathcal{N}(\mathbf{0}, \mathbf{I}_3)$ is the Gaussian distribution for translations, and $\mathcal{Q}_0 = \mathcal{IG}_{\text{SO}(3)}$ is the isotropic Gaussian distribution on $\text{SO}(3)$ for rotations [18], corresponding to uniformly sampling rotation axis $\mathbf{u} \in \mathbb{S}^2$ and rotation angle $\phi \in [0, \pi]$. Based on Eq. 2, we convert the sampled axis and angle to \mathbf{q}_0 . When $t = 1$, the ending points of these two flows, denoted as $\mathbf{T}_1 = (\mathbf{x}_1, \mathbf{q}_1)$, should be the transformation of a frame. We denote the data distribution of \mathbf{T}_1 as $\mathcal{T}_1 \times \mathcal{Q}_1$.

Linear Interpolation of Translation. For $\mathbf{x}_0 \sim \mathcal{T}_0$ and $\mathbf{x}_1 \sim \mathcal{T}_1$, we can interpolate the trajectory between them linearly: for $t \in [0, 1]$,

$$\mathbf{x}_t = (1 - t)\mathbf{x}_0 + t\mathbf{x}_1, \text{ with constant translation velocity: } \mathbf{v} = \mathbf{x}_1 - \mathbf{x}_0. \quad (7)$$

SLERP of Rotation in Exponential Format. For unit quaternions $\mathbf{q}_0 \sim \mathcal{Q}_0$ and $\mathbf{q}_1 \sim \mathcal{Q}_1$, we interpolate the trajectory between them via SLERP in an exponential format [28]:

$$\mathbf{q}_t = \mathbf{q}_0 \otimes \exp(t \log(\mathbf{q}_0^{-1} \otimes \mathbf{q}_1)), \text{ with constant angular velocity: } \boldsymbol{\omega} = \phi \mathbf{u}. \quad (8)$$

Here, $\mathbf{q}_0^{-1} \otimes \mathbf{q}_1 = [\cos(\phi/2), \sin(\phi/2) \mathbf{u}^\top]^\top$ and $\boldsymbol{\omega} = 2 \log(\mathbf{q}_0^{-1} \otimes \mathbf{q}_1)$. $\exp(\cdot)$ and $\log(\cdot)$ are exponential and logarithmic maps defined in Eq. 2 and Eq. 3, respectively.

Training QFlow Model. In this study, we adopt the SE(3)-equivariant neural network in FrameFlow [34], denoted as \mathcal{M}_θ , to model the flows. Given the transformation at time t , i.e., \mathbf{T}_t , the model predicts the transformation at $t = 1$:

$$\mathbf{T}_{\theta,1} = (\mathbf{x}_{\theta,1}, \mathbf{q}_{\theta,1}) = \mathcal{M}_\theta(\mathbf{T}_t, t). \quad (9)$$

We train this model by the proposed quaternion flow (QFlow) matching method. In particular, given the frame $\mathbf{T}_1 = (\mathbf{x}_1, \mathbf{q}_1)$, we first sample a timestamp $t \sim \text{Uniform}([0, 1])$ and random initial points $\mathbf{T}_0 = (\mathbf{x}_0, \mathbf{q}_0) \sim \mathcal{T}_0 \times \mathcal{Q}_0$. Then, we derive obtain $(\mathbf{x}_t, \mathbf{v})$ and $(\mathbf{q}_t, \boldsymbol{\omega})$ via Eq. 7 and Eq. 8, respectively. Passing $(\mathbf{x}_t, \mathbf{q}_t, t)$ through the model \mathcal{M}_θ , we obtain $\mathbf{x}_{\theta,1}$ and $\mathbf{q}_{\theta,1}$, and derive the translation and angular velocities at time t by

$$\mathbf{v}_{\theta,t} = \frac{\mathbf{x}_{\theta,1} - \mathbf{x}_t}{1 - t}, \quad \boldsymbol{\omega}_{\theta,t} = \frac{2 \log(\mathbf{q}_t^{-1} \otimes \mathbf{q}_{\theta,1})}{1 - t}. \quad (10)$$

Based on the constancy of the velocities, we train the model \mathcal{M}_θ by minimizing the following two objectives:

$$\mathcal{L}_{\mathbb{R}^3} = \mathbb{E}_{t, \mathcal{T}_0, \mathcal{T}_1} [\|\mathbf{v} - \mathbf{v}_{\theta,t}\|^2], \quad \mathcal{L}_{\text{SO}(3)} = \mathbb{E}_{t, \mathcal{Q}_0, \mathcal{Q}_1} [\|\boldsymbol{\omega} - \boldsymbol{\omega}_{\theta,t}\|^2]. \quad (11)$$

Besides the above MSE losses, we further consider the auxiliary loss proposed in [35], which discourages physical violations, e.g., chain breaks or steric clashes. Therefore, we train the model by

$$\min_\theta \mathcal{L}_{\mathbb{R}^3} + \mathcal{L}_{\text{SO}(3)} + \alpha \cdot \mathbf{1}\{t < \epsilon\} \cdot \mathcal{L}_{\text{aux}}, \quad (12)$$

where $\alpha \geq 0$ is the weight of the auxiliary loss, $\mathbf{1}$ is an indicator, signifying that the auxiliary loss is applied only when t is sampled below a predefined threshold ϵ .

Inference Based on QFlow. Given a trained model, we can generate frames of residues from noise with the predicted velocities. In particular, given initial $(\mathbf{x}_0, \mathbf{q}_0) \sim \mathcal{T}_0 \times \mathcal{Q}_0$, the translation is generated by an Euler solver with L steps:

$$\mathbf{x}_{t+\Delta t} = \mathbf{x}_t + \mathbf{v}_{\theta,t} \cdot \Delta t, \quad (13)$$

where the step size $\Delta t = \frac{1}{L}$. The quaternion of rotation is generated with an exponential step size scheduler: We modify Eq. 8, interpolating \mathbf{q}_t with an acceleration as

$$\mathbf{q}_t = \mathbf{q}_0 \otimes \exp((1 - e^{-\gamma t}) \log(\mathbf{q}_0^{-1} \otimes \mathbf{q}_1)), \quad (14)$$

where γ controls the rotation accelerating, and we empirically set $\gamma = 10$. Then, the Euler solver becomes:

$$\mathbf{q}_{t+\Delta t} = \mathbf{q}_t \otimes \exp\left(\frac{1}{2} \Delta t \cdot \gamma e^{-\gamma t} \boldsymbol{\omega}_{\theta,t}\right), \quad (15)$$

where $\gamma e^{-\gamma t} \boldsymbol{\omega}_{\theta,t}$ is the adjusted angular velocity. Previous works [2, 34] have demonstrated that the exponential step size scheduler helps reduce sampling steps and enhance model performance.

3.3 Rectified Quaternion Flow

Given the trained QFlow model \mathcal{M}_θ , we can rewire the flows in \mathbb{R}^3 and $\text{SO}(3)$, respectively, with a non-crossing manner by the flow rectification method in [23]. In particular, we generate noisy $\mathbf{T}'_0 = \{\mathbf{x}'_0, \mathbf{q}'_0\} \sim \mathcal{T}_0 \times \mathcal{Q}_0$ and transfer to $\mathbf{T}'_1 = \{\mathbf{x}'_1, \mathbf{q}'_1\} \sim \mathcal{T}_1 \times \mathcal{Q}_1$ by \mathcal{M}_θ . Taking \mathcal{M}_θ as the initialization, we use the noise-sample pairs, i.e., $\{\mathbf{T}'_0, \mathbf{T}'_1\}$, to train the model further by the same loss in Eq. 12 and derive the rectified QFlow (ReQFlow) model.

The work in [23] has demonstrated that the rectified flow of translation in \mathbb{R}^3 preserves the marginal law of the original translation flow and reduces the transport cost from the noise to the samples. We find that these theoretical properties are also held by the rectified quaternion flow under mild assumptions. Let $(\mathbf{q}_0, \mathbf{q}_1) \sim \mathcal{Q}_0 \times \mathcal{Q}_1$ be the pair used to train QFlow, and $(\mathbf{q}'_0, \mathbf{q}'_1)$ be the pair induced from $(\mathbf{q}_0, \mathbf{q}_1)$ by flow rectification. Then, we have

Theorem 3.1. (Marginal preserving property). *The pair $(\mathbf{q}'_0, \mathbf{q}'_1)$ is a coupling of \mathcal{Q}_0 and \mathcal{Q}_1 . The marginal law of \mathbf{q}'_t equals that of \mathbf{q}_t at everytime, that is $\text{Law}(\mathbf{q}'_t) = \text{Law}(\mathbf{q}_t)$.*

Theorem 3.2. (Reducing transport costs). *The pair $(\mathbf{q}'_0, \mathbf{q}'_1)$ yields lower or equal convex transport costs than the input $(\mathbf{q}_0, \mathbf{q}_1)$. For any convex $c: \mathbb{R}^3 \rightarrow \mathbb{R}$, define the cost as $C(\mathbf{q}_0, \mathbf{q}_1) = c(\log(\mathbf{q}_0^{-1} \otimes \mathbf{q}_1))$. Then, we have $\mathbb{E}[C(\mathbf{q}'_0, \mathbf{q}'_1)] \leq \mathbb{E}[C(\mathbf{q}_0, \mathbf{q}_1)]$.*

Theorem 3.2 shows that the coupling $(\mathbf{q}'_0, \mathbf{q}'_1)$ either achieves a strictly lower or the same convex transport cost compared to the original one, highlighting the advantage of the quaternion flow rectification in reducing the overall rotation displacement cost without compromising the marginal distribution constraints (Theorem 3.1). In addition, we have

Corollary 3.3. (Cost Reduction with Nonconstant Speed). *Suppose the geodesic interpolation \mathbf{q}_t between \mathbf{q}_0 and \mathbf{q}_1 has a constant axis \mathbf{u} , but its speed is nonconstant in time, i.e., $\boldsymbol{\omega}_t = a(t)\mathbf{u}$. The quaternion flow rectification still reduces or preserves the transport cost.*

This corollary means that when applying the exponential step size scheduler (i.e., Eq. 15), the rectification still reduces or preserves the transport cost.

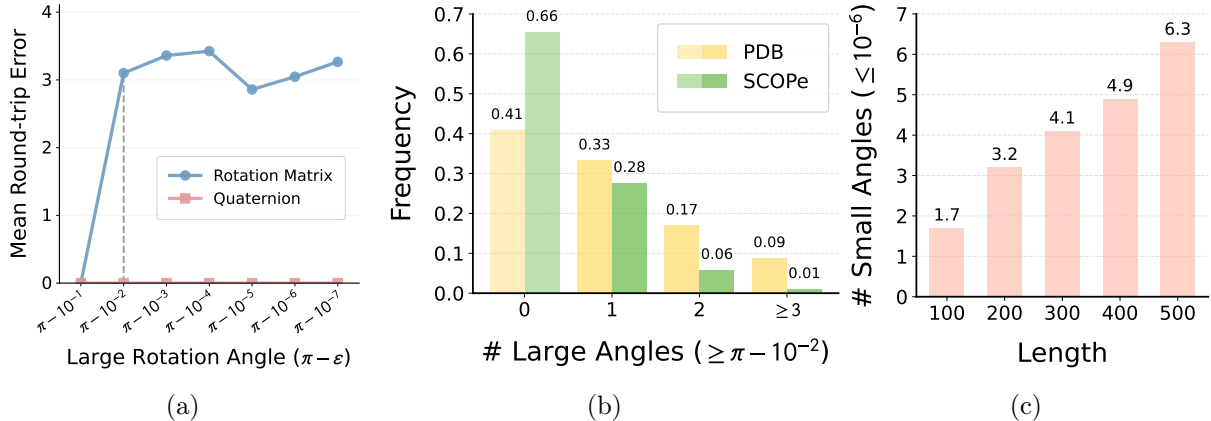


Figure 3: (a) Mean round-trip errors from $\pi - 10^{-1}$ to $\pi - 10^{-7}$. (b) The frequency of suffering large rotation angles per protein when training on the two datasets. (c) The average number of small rotation angles per protein when generating ten backbones for each length.

3.4 Rationality Analysis

Most existing methods, like FrameFlow [34] and FoldFlow [2], represent rotations as 3×3 matrices. Given two rotation matrices \mathbf{R}_0 and \mathbf{R}_1 , they construct a flow in $\text{SO}(3)$ with matrix geodesic interpolation:

$$\mathbf{R}_t = \mathbf{R}_0 \exp_M \left(t \log_M(\mathbf{R}_0^\top \mathbf{R}_1) \right), \quad (16)$$

where $\exp_M(\cdot)$ and $\log_M(\cdot)$ denote the matrix exponential and logarithmic maps, respectively. The corresponding angular velocity $\boldsymbol{\Omega} = \log_M(\mathbf{R}_0^\top \mathbf{R}_1)$. Different from existing methods [34, 35, 2], our method applies quaternion-based rotation representation and achieves rotation interpolation by SLERP in an exponential format, which achieves superior numerical stability and thus benefits protein backbone generation.

To verify this claim, we conduct a round-trip error experiment: given an rotation $\boldsymbol{\omega}$ in the axis-angle format, we convert it to a rotation matrix \mathbf{R} and a quaternion \mathbf{q} , respectively, and convert it back to the axis-angle format, denoted as $\hat{\boldsymbol{\omega}}_R$ and $\hat{\boldsymbol{\omega}}_q$, respectively. Figure 3a shows the round-trip errors in L_2 norm for large rotation angles (e.g., $\phi \in [\pi - 10^{-2}, \pi)$). Our quaternion-based method is numerically stable while the matrix-based representation suffers severe numerical errors. When training a protein backbone generation model, the numerical stability for large rotation angles is important. Given the frames in the Protein Data Bank (PDB) [3] dataset and the SCOPe [4] dataset, we sample a random noise for each frame and calculate the rotation angle between them. The histogram in Figure 3b shows that when training an arbitrary flow-based model, the probability of suffering at least one large angle per protein is 0.59 for PDB and 0.34 for SCOPe, respectively. It means that the matrix-based representation may introduce undesired numerical errors that aggregate and propagate during training.

In addition, a very recent work, AssembleFlow [8], also applies quaternion-based rotation representation and SLERP when modeling 3D molecules. In particular, it applies SLERP in an additive format:

$$\mathbf{q}_t = \frac{\sin((1-t)\frac{\phi}{2})}{\sin(\frac{\phi}{2})} \mathbf{q}_0 + \frac{\sin(t\frac{\phi}{2})}{\sin(\frac{\phi}{2})} \mathbf{q}_1, \quad (17)$$

Table 1: Comparisons for various rotation interpolation methods.

Method		Matrix Geodesic	SLERP (Add. Format)	SLERP (Exp. Format)
Interpolation	Formula	$\mathbf{R}_0 \exp_M(t \log_M(\mathbf{R}_0^\top \mathbf{R}_1))$	$\frac{\sin((1-t)\frac{\phi}{2})}{\sin\frac{\phi}{2}}\mathbf{q}_0 + \frac{\sin(t\frac{\phi}{2})}{\sin\frac{\phi}{2}}\mathbf{q}_1$	$\mathbf{q}_0 \otimes \exp(t \log(\mathbf{q}_0^{-1} \otimes \mathbf{q}_1))$
	Velocity	$\mathbf{\Omega} = \log_M(\mathbf{R}_0^\top \mathbf{R}_1)$	$\boldsymbol{\eta}_t = \frac{\phi(\cos(\frac{t\phi}{2})\mathbf{q}_1 - \cos((1-t)\frac{\phi}{2})\mathbf{q}_0)}{2 \sin\frac{\phi}{2}}$	$\boldsymbol{\omega} = 2 \log(\mathbf{q}_0^{-1} \otimes \mathbf{q}_1)$
Euler Solver	Update	$\mathbf{R}_{t+\Delta t} = \mathbf{R}_t \exp_M(\Delta t \cdot \mathbf{\Omega})$	$\mathbf{q}_{t+\Delta t} = \mathbf{q}_t + \Delta t \cdot \boldsymbol{\eta}_t$	$\mathbf{q}_{t+\Delta t} = \mathbf{q}_t \otimes \exp(\frac{1}{2} \Delta t \cdot \boldsymbol{\omega})$
	No Renormalization	✓	✗	✓
Numerical Stability	$\phi \geq \pi - 10^{-2}$	✗	✓	✓
	$\phi \leq 10^{-6}$	✓	✗	✓
Application Scenarios		FrameFlow [34], FoldFlow [2]	AssembleFlow [8]	QFlow (Ours), ReQFlow (Ours)

and updates rotations linearly by the following Euler solver:

$$\mathbf{q}_{t+\Delta t} = \mathbf{q}_t + \Delta t \cdot \boldsymbol{\eta}_t. \tag{18}$$

Here, $\boldsymbol{\eta}_t$ is the instantaneous velocity in the tangent space of \mathbf{q}_t , which is derived by the first-order derivative of Eq. 17. However, this modeling strategy also suffers numerical issues. Firstly, although the additive format SLERP can generate the same interpolation path as ours in theory, when rotation angle ϕ is small (e.g., $\phi \in [0, 10^{-6})$), Eq. 17 often outputs “NaN” because the denominator $\sin(\frac{\phi}{2})$ tends to zero. The exponential step size scheduler leads to rapid convergence when generating protein backbones, which frequently generates rotation angles below the threshold 10^{-6} (as shown in Figure 3c) and thus makes the additive format SLERP questionable in our task. Secondly, the Euler step in Eq. 18 makes $\|\mathbf{q}_{t+\Delta t}\|_2 \neq 1$, so that renormalization is required after each update. Table 1 provides a comprehensive comparison for the three rotation interpolation methods, highlighting the advantages of our method.

4 Experiment

To demonstrate the effectiveness and efficiency of our methods (QFlow and ReQFlow), we conduct comprehensive experiments to compare them with state-of-the-art protein backbone generation methods. In addition, we conduct ablation studies to verify the usefulness of the flow rectification strategy and the impact of sampling steps on model performance. All the experiments are implemented on four NVIDIA A100 80G GPUs. Implementation details and experimental results are shown in this section and Appendix C.

4.1 Experimental Setup

Datasets. We apply two commonly used datasets in our experiments. The first is the 23,366 protein backbones collected from Protein Data Bank (PDB) [3], whose lengths range from 60 to 512. The second is the SCOPE dataset [4] pre-processed by FrameFlow [34], which contains 3,673 protein backbones with lengths ranging from 60 to 128.

Baselines. The baselines of our methods include diffusion-based methods (FrameDiff [35], RFDiffusion [32], and Genie2 [20]) and flow-based methods (FrameFlow [34], FoldFlow [2], and FoldFlow2 [11]). In addition, we rectify FrameFlow by our method (i.e., re-training FrameFlow based on the paired data generated by itself) and consider the rectified FrameFlow (ReFrameFlow) as a baseline as well.

Table 2: Comparisons for various models on PDB. For each designability metric, we bold the best result and show the top-3 results with a blue background. In the same way, we indicate the best and top-3 diversity and novelty results among the rows with Fraction > 0.8. The inference time corresponds to generating a protein backbone with length $N = 300$.

Method	Efficiency		Designability		Diversity	Novelty
	Step	Time(s)	Fraction \uparrow	scRMSD \downarrow	TM \downarrow	TM \downarrow
RFDiffusion	50	66.23	0.904	1.102 \pm 1.617	0.382	0.822
Genie2	1000	112.93	0.908	1.132 \pm 1.389	0.370	0.759
	500	55.86	0.000	18.169 \pm 5.963	-	0.115
FrameDiff	500	48.12	0.564	2.936 \pm 3.093	0.441	0.799
FoldFlow _{Base}	500	43.52	0.624	3.080 \pm 3.449	0.469	0.870
FoldFlow _{SFM}	500	43.63	0.636	3.031 \pm 3.589	0.411	0.848
FoldFlow _{OT}	500	43.35	0.852	1.760 \pm 2.593	0.434	0.857
FoldFlow2	50	6.35	0.952	1.083 \pm 1.308	0.373	0.813
	20	2.63	0.644	3.060 \pm 3.210	0.339	0.736
FrameFlow	500	20.72	0.872	1.380 \pm 1.392	0.346	0.803
	200	8.69	0.864	1.542 \pm 1.889	0.348	0.809
	100	4.20	0.708	2.167 \pm 2.373	0.332	0.806
	50	2.23	0.704	2.639 \pm 3.079	0.334	0.791
	20	0.84	0.436	4.652 \pm 4.390	0.319	0.772
	10	0.47	0.180	7.343 \pm 5.125	0.317	0.762
QFlow	500	17.52	0.936	1.163 \pm 0.938	0.356	0.821
	200	6.85	0.864	1.400 \pm 1.259	0.344	0.807
	100	3.45	0.916	1.342 \pm 1.364	0.348	0.809
	50	1.87	0.812	1.785 \pm 2.151	0.344	0.784
	20	0.81	0.604	3.090 \pm 3.374	0.325	0.758
	10	0.45	0.332	5.032 \pm 4.303	0.313	0.715
ReQFlow	500	17.29	0.972	1.071\pm0.482	0.377	0.828
	200	7.44	0.932	1.160 \pm 0.782	0.384	0.826
	100	3.62	0.928	1.245 \pm 1.059	0.369	0.819
	50	1.81	0.912	1.254 \pm 0.915	0.369	0.810
	20	0.80	0.872	1.418 \pm 0.998	0.355	0.791
	10	0.45	0.676	2.443 \pm 2.382	0.337	0.760

Implementation Details. For the PDB dataset, we utilize the checkpoints of baselines and reproduce the results shown in their papers. Given the QFlow trained on PDB, we generate 7,653 protein backbones with lengths in [60, 512] from noise and then train ReQFlow based on these noise-backbone pairs. For the SCOPe dataset, we train all the models from scratch. Given the QFlow trained on SCOPe, we generate 3,167 protein backbones with lengths in [60, 128] from noise and then train ReQFlow based on these noise-backbone pairs. When training ReQFlow, we apply structural data filtering, selecting training samples based on scRMSD ($\leq 2\text{\AA}$) and TM-score (≥ 0.9 for long-chain proteins) and removing proteins with excessive loops ($> 50\%$) or abnormally large radius of gyration (top 4%). ReFrameFlow is trained in the same way.

Evaluation Metrics. Following previous works, we evaluate each method in the following four aspects:

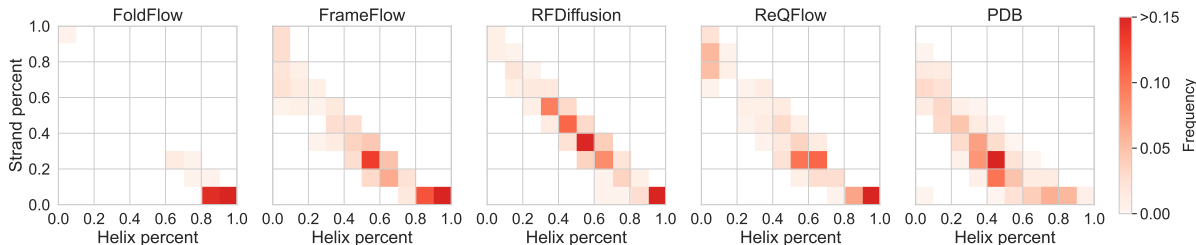


Figure 4: The distribution of protein backbones with respect to the percentages of their secondary structure.

1) Designability: As the most critical metric, designability reflects the possibility that a generated protein backbone can be realized by folding the corresponding amino acid sequence. It is assessed by the RMSD of C_α (i.e., scRMSD) between the generated protein backbone and the backbone predicted by ESMFold [21]. Given a set of generated backbones, we calculate the proportion of the backbones whose scRMSD $\leq 2\text{\AA}$ (denoted as Fraction).

2) Diversity:

Given designable protein backbones, whose scRMSD $\leq 2\text{\AA}$, we compute their pairwise TM-scores and assess the diversity by the average of the scores.

3) Novelty: For each designable protein backbone, we compute its maximum TM-score to the data in PDB using Foldseek [30]. The average of the scores reflect the novelty of the generated protein backbones.

4) Efficiency: We assess the computational efficiency of each method by the number of sampling steps and the inference time for generating 50 proteins at two lengths: 300 residues for PDB and 128 residues for SCOPe.

4.2 Comparison Experiments on PDB

Generation Quality. Given the models trained on PDB, we set the length of backbone $N \in \{100, 150, 200, 250, 300\}$, and generate 50 protein backbones for each length. Table 2 shows that ReQFlow achieves state-of-the-art performance in designability, achieving the highest Fraction (0.972) among all models, significantly outperforming strong competitors such as Genie2 (0.908) and RFDiffusion (0.904). Additionally, it achieves the lowest scRMSD (1.071 ± 0.482), with a notably smaller variance compared to the other methods, highlighting the model’s consistency and reliability in generating high-quality protein backbones. Meanwhile, ReQFlow maintains competitive performance in diversity and novelty (0.828), comparable to state-of-the-art baselines.

Computational Efficiency. Moreover, ReQFlow achieves ultra-fast protein backbone generation. Typically, ReQFlow achieves a high Fraction score (0.912) with merely 50 steps and 1.81s, outperforming RFDiffusion and Genie2 with $37\times$ and $62\times$ acceleration, respectively. The state-of-the-art methods like Genie2 and FoldFlow2 suffer severe performance degradation in designability when the number of steps is halved, while ReQFlow performs stably even reducing the number of steps from 500 to 20. In addition, even if using the same model architecture and inference setting, ReQFlow can be $\sim 10\%$ faster than FrameFlow because of utilizing the quaternion-based computation.

Fitness of Data Distribution. Given generated protein backbones, we record the percentages of

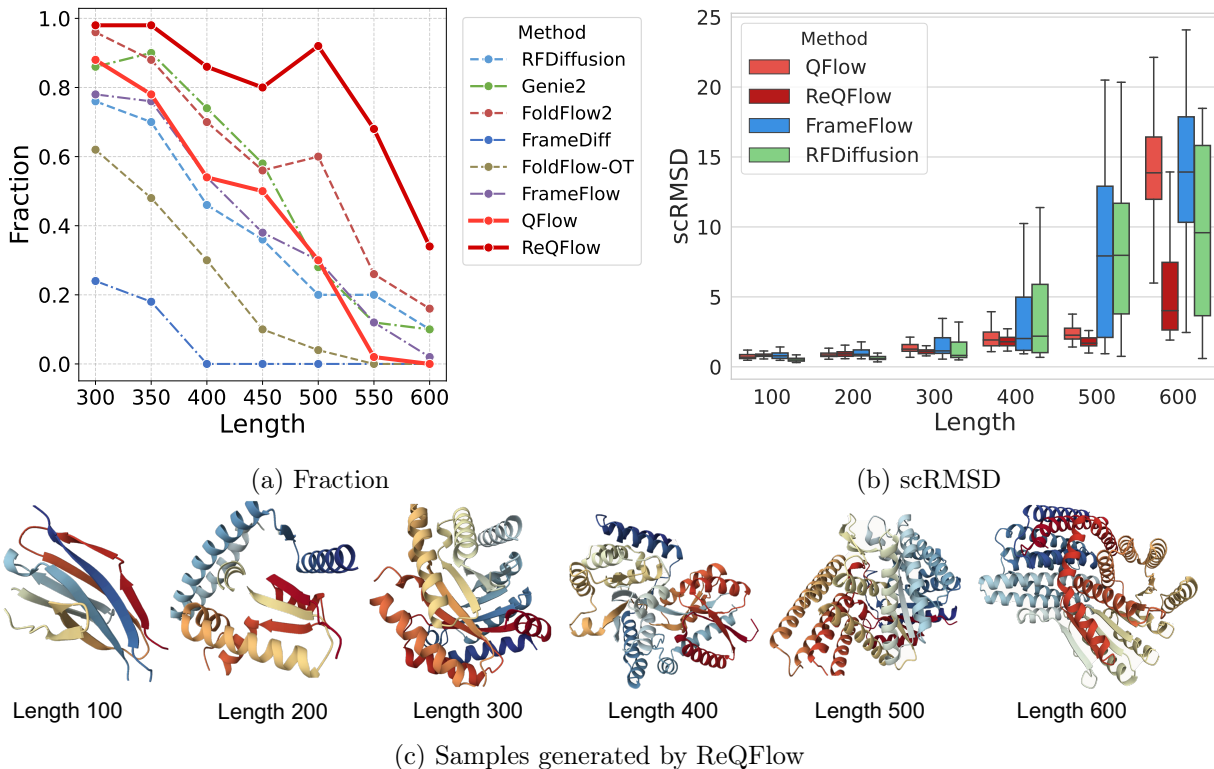


Figure 5: The comparison for various methods on the designability of generated long-chain protein backbones.

helix and strand, respectively, for each backbone, and visualize the distribution of the backbones with respect to the percentages in Figure 4. The protein backbones generated by ReQFlow have a reasonable distribution, which is similar to those of RFDiffusion and FrameFlow and comparable to that of the PDB dataset. However, the distribution of FoldFlow is significantly different from the data distribution and indicates a mode collapse risk — the protein backbones generated by FoldFlow are always dominated by helix structures. That is why FoldFlow is inferior to the other methods in diversity and novelty, as shown in Table 2.

Effectiveness on Long Chain Generation. Notably, ReQFlow demonstrates exceptional performance in generating long-chain protein backbones (e.g., $N > 300$). As shown in Figures 5a and 5b, ReQFlow outperforms all baselines on generating long protein backbones and shows remarkable robustness. Especially, when the length $N > 500$, which is out of the length range of PDB data, all the baselines fail to maintain high designability while ReQFlow still achieves promising performance in Fraction score and scRMSD and generates reasonable protein backbones, as shown in Figure 5c. This generalization ability beyond the training data distribution underscores ReQFlow’s potential for real-world applications requiring robust long-chain protein design.

Ablation Study. We conduct an ablation study to evaluate the impact of different components in the ReQFlow model. The results in Table 3 reveal that similar to existing methods [34, 2, 11], the exponential step size scheduler is important for ReQFlow, helping generate designable protein backbones with relatively few steps (e.g., $N \leq 500$). Additionally, the data filter is necessary for making flow rectification work. In particular, rectifying QFlow based on low-quality data leads to a substantial degradation in model performance. In contrast, after filtering out noisy and irrelevant

Table 3: The Fraction scores of ReQFlow under different settings when generating backbones with 300 residues by 500 steps.

Exponential Scheduler	Flow Rectification	Data Filtering	Sampling Steps		
			500	50	10
\times	\times	\times	0.040	0.004	0.004
\checkmark	\times	\times	0.936	0.812	0.332
\checkmark	\checkmark	\times	0.716	0.704	0.624
\checkmark	\checkmark	\checkmark	0.972	0.912	0.676

Table 4: Comparisons for various models on SCOPE. For each metric of generation quality, we indicate the best and top-3 results in the same way as Table 2 does. The inference time corresponds to generating a backbone with length $N = 128$.

Method	Efficiency		Designability		Diversity	Novelty
	Step	Time(s)	Fraction \uparrow	scRMSD \downarrow	TM \downarrow	TM \downarrow
FrameFlow	500	16.18	0.849	1.448 \pm 1.114	0.397	0.858
	50	1.69	0.820	1.546 \pm 1.316	0.379	0.836
	20	0.69	0.713	1.918 \pm 1.495	0.362	0.803
ReFrameFlow	500	16.24	0.897	1.368 \pm 1.412	0.403	0.857
	50	1.65	0.903	1.291 \pm 0.763	0.400	0.850
	20	0.68	0.871	1.416 \pm 0.880	0.401	0.846
QFlow	500	12.22	0.907	1.263 \pm 1.334	0.389	0.868
	50	1.33	0.872	1.389 \pm 1.314	0.371	0.863
	20	0.56	0.764	1.764 \pm 1.529	0.367	0.814
ReQFlow	500	12.18	0.972	1.043 \pm 0.416	0.416	0.868
	50	1.27	0.932	1.162 \pm 0.812	0.415	0.855
	20	0.51	0.929	1.214 \pm 0.633	0.404	0.844

data, rectifying QFlow based on the high-quality data boosts the model performance significantly.

4.3 Analytic Experiments on SCOPE

Universality of Flow Rectification. Note that, the flow rectification method used in our work is universal for various models. As shown in Table 4 and Figure 6, applying flow rectification, we can improve the efficiency and effectiveness of FrameFlow as well. This result highlights the broad utility of flow rectification as an operation that can enhance the performance of flow models on SO(3) spaces.

Superiority of Exponential-Format SLERP. The results in Table 4 and Figure 6 indicate that QFlow and ReQFlow outperform their corresponding counterparts (FrameFlow and ReFrameFlow) in terms of designability across all sampling steps. In addition, QFlow methods are approximately 25% faster than FrameFlow methods at each sampling step, demonstrating a significant speed advantage. As we analyzed in Section 3.4, the superiority of our models can be attributed to the better numerical stability and computational efficiency of quaternion calculations compared to the traditional matrix geodesic method.

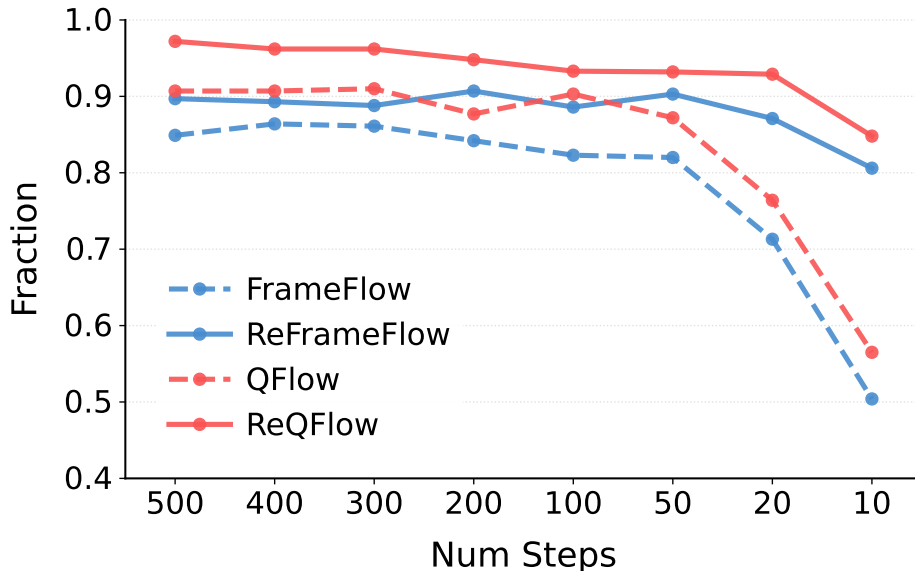


Figure 6: A comparison for various methods on their designability with the reduction of sampling steps. Original data is in Table 5.

5 Conclusion and Future Work

In this study, we propose a rectified quaternion flow matching method for efficient and high-quality protein backbone generation. Leveraging quaternion-based representation and flow rectification, our method achieves state-of-the-art performance and significantly reduces inference time. In the near future, we plan to improve our method for generating high-quality long-chain protein backbones, including constructing a larger training dataset, improving our model architecture, and leveraging the knowledge within large-scale pre-training models. As long-term goals, we will extend our method to conditional protein backbone generation for controllable protein design and explore its applications in side chain generation and full-atom protein generation.

References

- [1] Minkyung Baek, Frank DiMaio, Ivan Anishchenko, Justas Dauparas, Sergey Ovchinnikov, Gyu Rie Lee, Jue Wang, Qian Cong, Lisa N Kinch, R Dustin Schaeffer, et al. Accurate prediction of protein structures and interactions using a three-track neural network. *Science*, 373(6557):871–876, 2021.
- [2] Joey Bose, Tara Akhound-Sadegh, Guillaume Huguette, Kilian FATRAS, Jarrid Rector-Brooks, Cheng-Hao Liu, Andrei Cristian Nica, Maksym Korablyov, Michael M Bronstein, and Alexander Tong. Se (3)-stochastic flow matching for protein backbone generation. In *The Twelfth International Conference on Learning Representations*, 2024.
- [3] Stephen K Burley, Charmi Bhikadiya, Chunxiao Bi, Sebastian Bittrich, Henry Chao, Li Chen, Paul A Craig, Gregg V Crichlow, Kenneth Dalenberg, Jose M Duarte, et al. Rcsb protein data bank (rcsb.org): delivery of experimentally-determined pdb structures alongside one million computed structure models of proteins from artificial intelligence/machine learning. *Nucleic acids research*, 51(D1):D488–D508, 2023.

- [4] John-Marc Chandonia, Lindsey Guan, Shiangyi Lin, Changhua Yu, Naomi K Fox, and Steven E Brenner. Scope: improvements to the structural classification of proteins—extended database to facilitate variant interpretation and machine learning. *Nucleic acids research*, 50(D1):D553–D559, 2022.
- [5] Erik B Dam, Martin Koch, and Martin Lillholm. *Quaternions, interpolation and animation*, volume 2. Citeseer, 1998.
- [6] Justas Dauparas, Ivan Anishchenko, Nathaniel Bennett, Hua Bai, Robert J Ragotte, Lukas F Milles, Basile IM Wicky, Alexis Courbet, Rob J de Haas, Neville Bethel, et al. Robust deep learning–based protein sequence design using proteinmpnn. *Science*, 378(6615):49–56, 2022.
- [7] RA Engh and R Huber. Structure quality and target parameters. 2012.
- [8] Hongyu Guo, Yoshua Bengio, and Shengchao Liu. Assembleflow: Rigid flow matching with inertial frames for molecular assembly. In *The Thirteenth International Conference on Learning Representations*, 2025.
- [9] Evan G Hemingway and Oliver M O’Reilly. Perspectives on euler angle singularities, gimbal lock, and the orthogonality of applied forces and applied moments. *Multibody system dynamics*, 44:31–56, 2018.
- [10] Jonathan Ho, Ajay Jain, and Pieter Abbeel. Denoising diffusion probabilistic models. *Advances in neural information processing systems*, 33:6840–6851, 2020.
- [11] Guillaume Huguet, James Vuckovic, Kilian Fatras, Eric Thibodeau-Laufer, Pablo Lemos, Riashat Islam, Cheng-Hao Liu, Jarrid Rector-Brooks, Tara Akhound-Sadegh, Michael Bronstein, et al. Sequence-augmented se (3)-flow matching for conditional protein backbone generation. *arXiv preprint arXiv:2405.20313*, 2024.
- [12] John B Ingraham, Max Baranov, Zak Costello, Karl W Barber, Wujie Wang, Ahmed Ismail, Vincent Frappier, Dana M Lord, Christopher Ng-Thow-Hing, Erik R Van Vlack, et al. Illuminating protein space with a programmable generative model. *Nature*, 623(7989):1070–1078, 2023.
- [13] John Jumper, Richard Evans, Alexander Pritzel, Tim Green, Michael Figurnov, Olaf Ronneberger, Kathryn Tunyasuvunakool, Russ Bates, Augustin Židek, Anna Potapenko, et al. Highly accurate protein structure prediction with alphafold. *Nature*, 596(7873):583–589, 2021.
- [14] Wolfgang Kabsch and Christian Sander. Dictionary of protein secondary structure: pattern recognition of hydrogen-bonded and geometrical features. *Biopolymers: Original Research on Biomolecules*, 22(12):2577–2637, 1983.
- [15] Stephen A Kelly, Stefan Mix, Thomas S Moody, and Brendan F Gilmore. Transaminases for industrial biocatalysis: novel enzyme discovery. *Applied microbiology and biotechnology*, 104:4781–4794, 2020.
- [16] Jonas Köhler, Michele Invernizzi, Pim De Haan, and Frank Noé. Rigid body flows for sampling molecular crystal structures. In *International Conference on Machine Learning*, pages 17301–17326. PMLR, 2023.
- [17] Jack B Kuipers. *Quaternions and rotation sequences: a primer with applications to orbits, aerospace, and virtual reality*. Princeton university press, 1999.

- [18] Adam Leach, Sebastian M Schmon, Matteo T Degiacomi, and Chris G Willcocks. Denoising diffusion probabilistic models on so (3) for rotational alignment. In *ICLR Workshop on Geometrical and Topological Representation Learning*, 2022.
- [19] Yeqing Lin and Mohammed Alquraishi. Generating novel, designable, and diverse protein structures by equivariantly diffusing oriented residue clouds. In *International Conference on Machine Learning*, pages 20978–21002. PMLR, 2023.
- [20] Yeqing Lin, Minji Lee, Zhao Zhang, and Mohammed AlQuraishi. Out of many, one: Designing and scaffolding proteins at the scale of the structural universe with genie 2. *arXiv preprint arXiv:2405.15489*, 2024.
- [21] Zeming Lin, Halil Akin, Roshan Rao, Brian Hie, Zhongkai Zhu, Wenting Lu, Nikita Smetanin, Robert Verkuil, Ori Kabeli, Yaniv Shmueli, et al. Evolutionary-scale prediction of atomic-level protein structure with a language model. *Science*, 379(6637):1123–1130, 2023.
- [22] Yaron Lipman, Ricky TQ Chen, Heli Ben-Hamu, Maximilian Nickel, and Matthew Le. Flow matching for generative modeling. In *The Eleventh International Conference on Learning Representations*, 2023.
- [23] Qiang Liu. Rectified flow: A marginal preserving approach to optimal transport. *arXiv preprint arXiv:2209.14577*, 2022.
- [24] Edward Pervin and Jon A Webb. Quaternions in computer vision and robotics. 1982.
- [25] David Sehnal, Sebastian Bittrich, Mandar Deshpande, Radka Svobodová, Karel Berka, Václav Bazgier, Sameer Velankar, Stephen K Burley, Jaroslav Koča, and Alexander S Rose. Mol* viewer: modern web app for 3d visualization and analysis of large biomolecular structures. *Nucleic acids research*, 49(W1):W431–W437, 2021.
- [26] Ken Shoemake. Animating rotation with quaternion curves. *ACM SIGGRAPH Computer Graphics*, 19(3):245–254, 1985.
- [27] Daniel-Adriano Silva, Shawn Yu, Umut Y Ulge, Jamie B Spangler, Kevin M Jude, Carlos Labão-Almeida, Lestat R Ali, Alfredo Quijano-Rubio, Mikel Ruterbusch, Isabel Leung, et al. De novo design of potent and selective mimics of il-2 and il-15. *Nature*, 565(7738):186–191, 2019.
- [28] Joan Sola. Quaternion kinematics for the error-state kalman filter. *arXiv preprint arXiv:1711.02508*, 2017.
- [29] Simon J Teague. Implications of protein flexibility for drug discovery. *Nature reviews Drug discovery*, 2(7):527–541, 2003.
- [30] Michel van Kempen, Stephanie S Kim, Charlotte Tumescheit, Milot Mirdita, Cameron LM Gilchrist, Johannes Söding, and Martin Steinegger. Foldseek: fast and accurate protein structure search. *Biorxiv*, pages 2022–02, 2022.
- [31] Simon Wagner, Leif Seute, Vsevolod Viliuga, Nicolas Wolf, Frauke Gräter, and Jan Stuehmer. Generating highly designable proteins with geometric algebra flow matching. In *The Thirty-eighth Annual Conference on Neural Information Processing Systems*, 2024.
- [32] Joseph L Watson, David Juergens, Nathaniel R Bennett, Brian L Trippe, Jason Yim, Helen E Eisenach, Woody Ahern, Andrew J Borst, Robert J Ragothe, Lukas F Milles, et al. De novo design of protein structure and function with rfdiffusion. *Nature*, 620(7976):1089–1100, 2023.

- [33] Yi Xu, Licheng Yu, Hongteng Xu, Hao Zhang, and Truong Nguyen. Vector sparse representation of color image using quaternion matrix analysis. *IEEE Transactions on image processing*, 24(4):1315–1329, 2015.
- [34] Jason Yim, Andrew Campbell, Andrew YK Foong, Michael Gastegger, José Jiménez-Luna, Sarah Lewis, Victor Garcia Satorras, Bastiaan S Veeling, Regina Barzilay, Tommi Jaakkola, et al. Fast protein backbone generation with se (3) flow matching. *arXiv preprint arXiv:2310.05297*, 2023.
- [35] Jason Yim, Brian L Trippe, Valentin De Bortoli, Emile Mathieu, Arnaud Doucet, Regina Barzilay, and Tommi Jaakkola. Se (3) diffusion model with application to protein backbone generation. In *Proceedings of the 40th International Conference on Machine Learning*, pages 40001–40039, 2023.
- [36] Angxiao Yue, Dixin Luo, and Hongteng Xu. A plug-and-play quaternion message-passing module for molecular conformation representation. In *Proceedings of the AAAI Conference on Artificial Intelligence*, volume 38, pages 16633–16641, 2024.
- [37] Xuan Zhang, Shaofei Qin, Yi Xu, and Hongteng Xu. Quaternion product units for deep learning on 3d rotation groups. In *Proceedings of the IEEE/CVF conference on computer vision and pattern recognition*, pages 7304–7313, 2020.
- [38] Yongheng Zhao, Tolga Birdal, Jan Eric Lenssen, Emanuele Menegatti, Leonidas Guibas, and Federico Tombari. Quaternion equivariant capsule networks for 3d point clouds. In *Computer Vision–ECCV 2020: 16th European Conference, Glasgow, UK, August 23–28, 2020, Proceedings, Part I 16*, pages 1–19. Springer, 2020.
- [39] Xuanyu Zhu, Yi Xu, Hongteng Xu, and Changjian Chen. Quaternion convolutional neural networks. In *Proceedings of the European conference on computer vision*, pages 631–647, 2018.

A Proofs of Key Theoretical Results

A.1 The Angular Velocity under Exponential Scheduler

Proposition A.1. *For spherical linear interpolation (SLERP) with angular velocity $\boldsymbol{\omega}$, when applying an exponential scheduler during inference:*

$$\mathbf{q}_t = \mathbf{q}_0 \otimes \exp\left((1 - e^{-\gamma t}) \log(\mathbf{q}_0^{-1} \otimes \mathbf{q}_1)\right), \quad (19)$$

the resulting angular velocity evolves as $\hat{\boldsymbol{\omega}}_t = \gamma e^{-\gamma t} \boldsymbol{\omega}$.

Proof. The standard SLERP formulation in exponential form is:

$$\mathbf{q}_t = \mathbf{q}_0 \otimes \exp\left(t \log(\mathbf{q}_0^{-1} \otimes \mathbf{q}_1)\right), \quad (20)$$

where the relative rotation $\mathbf{q}_{\text{rel}} = \mathbf{q}_0^{-1} \otimes \mathbf{q}_1$ has logarithm map $\log(\mathbf{q}_{\text{rel}}) = \frac{1}{2} \phi \mathbf{u}$. The angular velocity is:

$$\boldsymbol{\omega} = 2 \cdot \log(\mathbf{q}_{\text{rel}}) = \phi \mathbf{u}. \quad (21)$$

Introducing an exponential scheduler $\kappa(t) = 1 - e^{-\gamma t}$ with derivative $\kappa'(t) = \gamma e^{-\gamma t}$, the modified SLERP becomes:

$$\mathbf{q}_t = \mathbf{q}_0 \otimes \exp\left(\kappa(t) \log(\mathbf{q}_{\text{rel}})\right). \quad (22)$$

Differentiating with respect to time using the chain rule:

$$\begin{aligned} \dot{\mathbf{q}}_t &= \mathbf{q}_0 \otimes \frac{d}{dt} \exp\left(\kappa(t) \log(\mathbf{q}_{\text{rel}})\right) \\ &= \gamma e^{-\gamma t} \log(\mathbf{q}_{\text{rel}}) \otimes \mathbf{q}_0 \otimes \exp\left(\kappa(t) \log(\mathbf{q}_{\text{rel}})\right) \\ &= \gamma e^{-\gamma t} \log(\mathbf{q}_{\text{rel}}) \otimes \mathbf{q}_t. \end{aligned} \quad (23)$$

Applying the quaternion kinematics equation $\dot{\mathbf{q}} = \frac{1}{2} [0, \boldsymbol{\omega}^\top]^\top \otimes \mathbf{q}$ [28], we solve for the effective angular velocity:

$$\begin{aligned} [0, \hat{\boldsymbol{\omega}}_t^\top]^\top &= 2 \dot{\mathbf{q}}_t \otimes \mathbf{q}_t^{-1} \\ &= 2 \gamma e^{-\gamma t} \log(\mathbf{q}_{\text{rel}}) \otimes \mathbf{q}_t \otimes \mathbf{q}_t^{-1} \\ &= 2 \gamma e^{-\gamma t} \log(\mathbf{q}_{\text{rel}}). \end{aligned} \quad (24)$$

Substituting the angular velocity from Eq. 21 yields:

$$\hat{\boldsymbol{\omega}}_t = \gamma e^{-\gamma t} \boldsymbol{\omega}. \quad (25)$$

□

A.2 Proofs of The Theorems in Section 3.3

Our proofs yield the same pipeline used in [23]. The proofs are inspired by that work and derived based on the same techniques. What we did is extending and specifying the theoretical results in [23] for \mathbb{S}^3 . The original rotation process is $\{\mathbf{q}_t\}_{t \in [0,1]}$, where each \mathbf{q}_t is a unit quaternion representing a rotation in $\text{SO}(3)$, $\boldsymbol{\omega}_t \in \mathbb{R}^3$ is the angular velocity at time t . The quaternion dynamics are given by

$$\dot{\mathbf{q}}_t = \frac{1}{2} [0, \boldsymbol{\omega}_t^\top]^\top \otimes \mathbf{q}_t \in T_{\mathbf{q}_t}(\mathbb{S}^3), \quad (26)$$

where $T_{\mathbf{q}_t}(\mathbb{S}^3)$ is the tangent space at \mathbf{q}_t . We write $\mathbf{q}_0 \sim \mathcal{Q}_0$, $\mathbf{q}_1 \sim \mathcal{Q}_1$ for the initial and target distributions. For a given input coupling $(\mathbf{q}_0, \mathbf{q}_1)$, the exact minimum of $\mathcal{L}_{\text{SO}(3)}$ in Eq. 11 is achieved if

$$\tilde{\omega}_{\theta,t} = \tilde{\omega}_t(\mathbf{q}, t) = \mathbb{E}[\boldsymbol{\omega}_t | \mathbf{q}_t = \mathbf{q}] \in \mathbb{R}^3, \quad (27)$$

which is the expected angular velocity at point \mathbf{q} , time t . We now define the rectified process $\{\mathbf{q}'_t\}_{t \in [0,1]}$ by

$$\dot{\mathbf{q}}'_t = \frac{1}{2}[0, \tilde{\omega}_t(\mathbf{q}'_t, t)^\top]^\top \otimes \mathbf{q}'_t, \quad \mathbf{q}'_0 \sim \mathcal{Q}_0, \quad (28)$$

A.2.1 Proof of Theorems 3.1

Proof. Consider any smooth test function $h : \mathbb{S}^3 \rightarrow \mathbb{R}$. By chain rule:

$$\frac{d}{dt} \mathbb{E}[h(\mathbf{q}_t)] = \mathbb{E}[\nabla_{\mathbb{S}^3} h(\mathbf{q}_t) \cdot \dot{\mathbf{q}}_t], \quad (29)$$

where $\nabla_{\mathbb{S}^3} h$ is the gradient on the manifold. From the definition in Eq. 26, since $\boldsymbol{\omega}_t$ is random, we rewrite inside the expectation by conditioning on \mathbf{q}_t :

$$\mathbb{E}[\nabla_{\mathbb{S}^3} h(\mathbf{q}_t) \cdot \dot{\mathbf{q}}_t] = \mathbb{E}\left[\nabla_{\mathbb{S}^3} h(\mathbf{q}_t) \cdot \frac{1}{2}[0, \mathbb{E}(\boldsymbol{\omega}_t | \mathbf{q}_t)^\top]^\top \otimes \mathbf{q}_t\right], \quad (30)$$

because $\boldsymbol{\omega}_t | (\mathbf{q}_t = \mathbf{q})$ has conditional mean $\tilde{\omega}_t(\mathbf{q}, t)$,

$$\frac{d}{dt} \mathbb{E}[h(\mathbf{q}_t)] = \mathbb{E}\left[\nabla_{\mathbb{S}^3} h(\mathbf{q}_t) \cdot \frac{1}{2}[0, \tilde{\omega}_t(\mathbf{q}_t, t)^\top]^\top \otimes \mathbf{q}_t\right]. \quad (31)$$

This evolution is exactly the *weak (distributional) form* of the continuity equation:

$$\partial_t \mu_t + \nabla \cdot \left(\frac{1}{2}[0, \tilde{\omega}_t(\mathbf{q}, t)^\top]^\top \otimes \mathbf{q} \cdot \mu_t\right) = 0, \quad (32)$$

where $\mu_t = \text{Law}(\mathbf{q}_t)$. According to Eq. 28, That is exactly the same weak-form evolution equation satisfied by the \mathbf{q}'_t process, where $\boldsymbol{\omega}$ is simply replaced by $\tilde{\omega}_t$. If we let $\nu_t := \text{Law}(\mathbf{q}'_t)$, it solves the same continuity equation with the same initial data $\nu_0 = \mu_0$. On a compact manifold like $\text{SO}(3)$, the continuity equation has a unique solution given an initial distribution. Hence $\mu_t = \nu_t$ at all times t . That is,

$$\text{Law}(\mathbf{q}'_t) = \text{Law}(\mathbf{q}_t), \quad \text{for all } t \in [0, 1]. \quad (33)$$

□

A.2.2 Proof of Theorems 3.2

Proof. The net rotation from \mathbf{q}_0 to \mathbf{q}_1 can be given by integrating the angular velocity $\boldsymbol{\omega}_t \in \mathbb{R}^3$.

$$\log(\mathbf{q}_0^{-1} \otimes \mathbf{q}_1) = \frac{1}{2} \int_0^1 \boldsymbol{\omega}_t dt, \quad (34)$$

and similarly,

$$\log(\mathbf{q}'_0^{-1} \otimes \mathbf{q}'_1) = \frac{1}{2} \int_0^1 \tilde{\omega}_t(\mathbf{q}'_t, t) dt, \quad (35)$$

Strictly speaking, one must keep track of the axis direction to ensure consistency, but the geodesic assumption here handles that. The rectified angular velocity $\tilde{\omega}_t = \mathbb{E}[\boldsymbol{\omega}_t | \mathbf{q}_t]$ implies that the total rotation in the rectified process is a conditional expectation of the original rotation:

$$\log(\mathbf{q}'_0^{-1} \otimes \mathbf{q}'_1) = \frac{1}{2} \int_0^1 \tilde{\omega}_t dt = \frac{1}{2} \mathbb{E} \left[\int_0^1 \boldsymbol{\omega}_t dt \mid \{\mathbf{q}'_t\} \right]. \quad (36)$$

Applying Jensen's inequality to the convex cost c over this conditional expectation:

$$c(\log(\mathbf{q}'_0 \otimes \mathbf{q}'_1)) = c\left(\frac{1}{2}\mathbb{E}\left[\int_0^1 \boldsymbol{\omega}_t dt \mid \{\mathbf{q}'_t\}\right]\right) \leq \mathbb{E}\left[\frac{1}{2}c\left(\int_0^1 \boldsymbol{\omega}_t dt\right) \mid \{\mathbf{q}'_t\}\right]. \quad (37)$$

Taking the total expectation on both sides:

$$\mathbb{E}[C(\mathbf{q}'_0, \mathbf{q}'_1)] \leq \mathbb{E}\left[\frac{1}{2}c\left(\int_0^1 \boldsymbol{\omega}_t dt\right)\right] = \mathbb{E}[C(\mathbf{q}_0, \mathbf{q}_1)]. \quad (38)$$

This final inequality establishes that the rectified coupling $(\mathbf{q}'_0, \mathbf{q}'_1)$ achieves equal or lower expected transport cost than the original coupling $(\mathbf{q}_0, \mathbf{q}_1)$. □

A.2.3 Proof of Corollary 3.3

Proof. Suppose the original process has the nonconstant angular velocity $\boldsymbol{\omega}_t = a(t)\mathbf{u}$ (fixed axis), with $\tau = \frac{1}{2}\int_0^1 a(t)dt$.

$$\log(\mathbf{q}_0^{-1} \otimes \mathbf{q}_1) = \frac{1}{2}\int_0^1 \boldsymbol{\omega}_t dt = \frac{1}{2}\mathbf{u}\int_0^1 a(t) dt = \tau\mathbf{u} \quad (39)$$

Recall that the rectified angular velocity is:

$$\tilde{\boldsymbol{\omega}}_t(\mathbf{q}, t) = \mathbb{E}[\boldsymbol{\omega}_t | \mathbf{q}_t] \quad (40)$$

Since $\boldsymbol{\omega}_t = a(t)\mathbf{u}$, we simply get:

$$\tilde{\boldsymbol{\omega}}_t(\mathbf{q}, t) = \mathbb{E}[a(t) | \mathbf{q}_t]\mathbf{u} \quad (41)$$

The total rotation from \mathbf{q}'_0 to the \mathbf{q}'_1 in the rectified process satisfies:

$$\log(\mathbf{q}'_0 \otimes \mathbf{q}'_1) = \frac{1}{2}\int_0^1 \tilde{\boldsymbol{\omega}}_t(\mathbf{q}'_t, t)dt = \frac{1}{2}\left(\int_0^1 \mathbb{E}[a(t) | \mathbf{q}'_t]dt\right)\mathbf{u}. \quad (42)$$

Let $\tau' = \frac{1}{2}\int_0^1 \mathbb{E}[a(t) | \mathbf{q}'_t]dt$. Thus,

$$\log(\mathbf{q}'_0 \otimes \mathbf{q}'_1) = \tau'\mathbf{u} \quad (43)$$

Because $\tau = \frac{1}{2}\int_0^1 a(t)dt$, $\tau' = \frac{1}{2}\int_0^1 \mathbb{E}[a(t) | \mathbf{q}_t]dt$, and Eq. 36 in Theorem 3.2, we note

$$\tau'\mathbf{u} = \frac{1}{2}\mathbf{u}\left(\int_0^1 \mathbb{E}[a(t) | \mathbf{q}'_t]dt\right) = \frac{1}{2}\mathbb{E}\left[\int_0^1 a(t)\mathbf{u} dt \mid \{\mathbf{q}'_t\}\right] = \mathbb{E}[\tau\mathbf{u} | \{\mathbf{q}'_t\}] \quad (44)$$

For the coupling $(\mathbf{q}'_0, \mathbf{q}'_1)$, the cost is:

$$C(\mathbf{q}'_0, \mathbf{q}'_1) = c(\tau'\mathbf{u}). \quad (45)$$

Since $\tau'\mathbf{u} = \mathbb{E}[\tau\mathbf{u} | \{\mathbf{q}'_t\}]$, convexity of c implies Jensen's inequality in conditional form:

$$c(\tau'\mathbf{u}) = c(\mathbb{E}[\tau\mathbf{u} | \{\mathbf{q}'_t\}]) \leq \mathbb{E}[c(\tau\mathbf{u}) | \{\mathbf{q}'_t\}] \quad (46)$$

Next, take unconditional expectation on both sides. By the law of total expectation (tower property),

$$\mathbb{E}[c(\tau'\mathbf{u})] \leq \mathbb{E}[c(\tau\mathbf{u})]. \quad (47)$$

Since $c(\tau\mathbf{u}) = c(\log(\mathbf{q}_0^{-1} \otimes \mathbf{q}_1)) = C(\mathbf{q}_0, \mathbf{q}_1)$ and $c(\tau'\mathbf{u}) = C(\mathbf{q}'_0, \mathbf{q}'_1)$. Therefore,

$$\mathbb{E}[C(\mathbf{q}'_0, \mathbf{q}'_1)] \leq \mathbb{E}[C(\mathbf{q}_0, \mathbf{q}_1)]. \quad (48)$$

□

B Implementation Details

B.1 Ensuring The Shortest Geodesic Path on SO(3)

When we interpolate two quaternions by using SLERP in an exponential format (Eq. 8), due to the double-cover property of quaternions (where every 3D rotation is represented by two antipodal unit quaternions), it is possible that the inner product $\langle \mathbf{q}_0, \mathbf{q}_1 \rangle < 0$, which means that \mathbf{q}_0 and \mathbf{q}_1 lie in opposite hemispheres. In such a situation, we apply $-\mathbf{q}_1$ in Eq. 8, ensuring the shortest geodesic path on SO(3).

B.2 Auxiliary Loss

We adopt the auxiliary loss from [35] to discourage physical violations such as chain breaks or steric clashes. Let $\mathcal{A} = [\text{N}, \text{C}_\alpha, \text{C}, \text{O}]$ be the collection of backbone atoms. The first term penalizes deviations in backbone atom coordinates:

$$\mathcal{L}_{\text{bb}} = \frac{1}{4N} \sum_{n=1}^N \sum_{a \in \mathcal{A}} \|a_n - \hat{a}_n\|^2, \quad (49)$$

where a_n is the ground-truth atom position, \hat{a}_n is our predicted position, N represents the number of residues. The second loss is a local neighborhood loss on pairwise atomic distances,

$$\mathcal{L}_{\text{dis}} = \frac{1}{Z} \sum_{n,m=1}^N \sum_{a,b \in \mathcal{A}} \mathbf{1}\{d_{ab}^{nm} < 0.6\} \|d_{ab}^{nm} - \hat{d}_{ab}^{nm}\|^2, \quad (50)$$

$$Z = \left(\sum_{n,m=1}^N \sum_{a,b \in \mathcal{A}} \mathbf{1}\{d_{ab}^{nm} < 0.6\} \right) - N, \quad (51)$$

where $d_{ab}^{nm} = \|a_n - b_m\|$ and $\hat{d}_{ab}^{nm} = \|\hat{a}_n - \hat{b}_m\|$ represent true and predicted inter-atomic distances between atoms $a, b \in \mathcal{A}$ for residue n and m . $\mathbf{1}$ is an indicator, signifying that only penalize atoms within 0.6nm(6Å). The full auxiliary loss can be written as

$$\mathcal{L}_{\text{aux}} = \mathcal{L}_{\text{bb}} + \mathcal{L}_{\text{dis}}. \quad (52)$$

B.3 The Schemes of Training and Inference Algorithms

The schemes of our training and inference algorithms are shown below.

B.4 Data Statistics and Hyperparameter Settings

We follow [35] to construct PDB dataset. The dataset was downloaded on December 17, 2024. We then applied a length filter (60–512 residues) and a resolution filter ($< 5 \text{ \AA}$) to select high-quality structures. To further refine the dataset, we processed each monomer using DSSP [14], removing those with more than 50% loops to ensure high secondary structure content. After filtering, 23,366 proteins remained for training. We directly use the SCOPe dataset preprocessed by [34] for training, which consists of 3,673 proteins after filtering. The distribution of dataset length is shown on Figure 7.

When conducting reflow, we first generated a large amount of data to create the training dataset and then applied filtering to refine it. The filtering criteria were as follows: for proteins with lengths

Algorithm 1 Training Procedure of QFlow

Require: Training dataset $T_1^D = \{\{T_1^j = (\mathbf{x}_1^j, \mathbf{q}_1^j)\}_{j=1}^{N_i}\}_{i=1}^D$, model \mathcal{M}_θ , number of epochs N

- 1: Initialize model parameters θ
- 2: **for** epoch = 1 to N **do**
- 3: **for** each mini-batch $T_1^B \subset T_1^D$ **do**
- 4: Sample $t^B \sim \mathcal{U}[0, 1]$, $T_0^B \sim \mathcal{T}_0 \times \mathcal{Q}_0$
- 5: Interpolate translations: $\mathbf{x}_t^B = \text{Linear}(\mathbf{x}_0^B, \mathbf{x}_1^B, t^B)$ Eq. 7
- 6: Interpolate rotations: $\mathbf{q}_t^B = \text{SLERP-Exp}(\mathbf{q}_0^B, \mathbf{q}_1^B, t^B)$ Eq. 8
- 7: Predict targets: $\mathbf{x}_{\theta,1}^B, \mathbf{q}_{\theta,1}^B = \mathcal{M}_\theta(T_t^B, t^B)$
- 8: Compute loss $\mathcal{L}(\theta; \mathbf{x}_t^B, \mathbf{q}_t^B, \mathbf{x}_{\theta,1}^B, \mathbf{q}_{\theta,1}^B)$ Eq. 12
- 9: Compute gradient $\nabla_\theta \mathcal{L}$
- 10: Update parameters: $\theta \leftarrow \theta - \eta \nabla_\theta \mathcal{L}$
- 11: **end for**
- 12: **end for**
- 13: **Return:** Trained model parameters θ^*

Algorithm 2 Inference

Require: Trained model \mathcal{M}_θ , random noise $T_0 \sim \mathcal{T}_0 \times \mathcal{Q}_0$, number of steps L , rotation acceleration constant γ

- 1: Initialize $t = 0$, $\Delta t = \frac{1}{L}$
- 2: **for** step = 1 to L **do**
- 3: Predict targets: $\mathbf{x}_{\theta,1}, \mathbf{q}_{\theta,1} = \mathcal{M}_\theta(T_t, t)$
- 4: Compute velocity: $\mathbf{v}_{\theta,t}, \boldsymbol{\omega}_{\theta,t}$ Eq. 10
- 5: Update translations: $\mathbf{x}_{t+\Delta t} \leftarrow \mathbf{x}_t + \mathbf{v}_{\theta,t} \cdot \Delta t$ Eq. 13
- 6: Update rotations: $\mathbf{q}_{t+\Delta t} \leftarrow \mathbf{q}_t \otimes \exp\left(\frac{1}{2}\Delta t \cdot \gamma e^{-\gamma t} \boldsymbol{\omega}_{\theta,t}\right)$ Eq. 15
- 7: Update states: $t \leftarrow t + \Delta t$, $T_t \leftarrow T_{t+\Delta t}$
- 8: **end for**
- 9: **Return:** generated backbone frame T_1

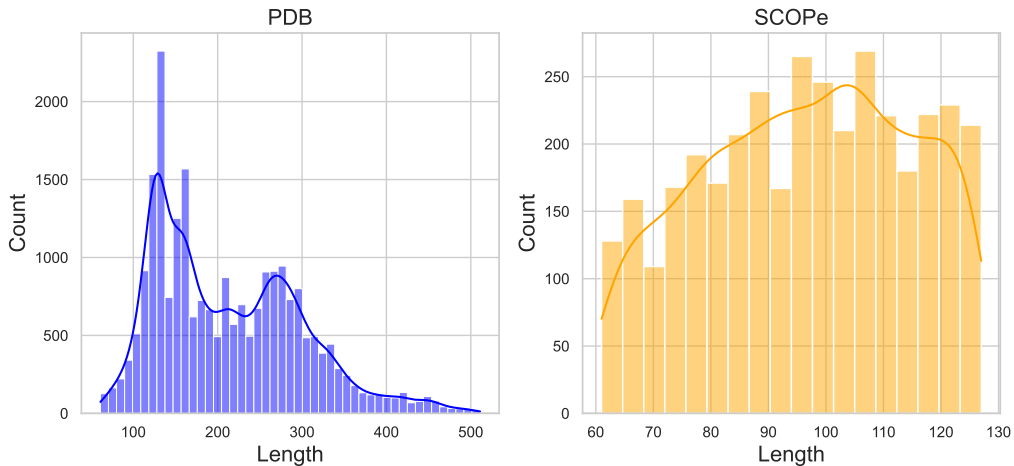


Figure 7: The length distribution of PDB and SCOPe dataset we use for training.

Algorithm 3 Training Procedure of ReQFlow

Require: Trained QFlow model \mathcal{M}_θ , number of epochs N

- 1: Sample noise $T_0^{\prime\mathcal{D}} \sim \mathcal{T}_0 \times \mathcal{Q}_0$
 - 2: Create flow rectification pairs: $(T'_0, T'_1)^{\mathcal{D}}$ Alg. 2
 - 3: **for** epoch = 1 to N **do**
 - 4: **for** each mini-batch $(T'_0, T'_1)^{\mathcal{B}} \subset (T'_0, T'_1)^{\mathcal{D}}$ **do**
 - 5: Sample $t^{\mathcal{B}} \sim \mathcal{U}[0, 1]$
 - 6: Interpolate translations: $\mathbf{x}'_t^{\mathcal{B}} = \text{Linear}(\mathbf{x}'_0^{\mathcal{B}}, \mathbf{x}'_1^{\mathcal{B}}, t^{\mathcal{B}})$ Eq. 7
 - 7: Interpolate rotations: $\mathbf{q}'_t^{\mathcal{B}} = \text{SLERP-Exp}(\mathbf{q}'_0^{\mathcal{B}}, \mathbf{q}'_1^{\mathcal{B}}, t^{\mathcal{B}})$ Eq. 8
 - 8: Predict targets: $\mathbf{x}'_{\theta,1}^{\mathcal{B}}, \mathbf{q}'_{\theta,1}^{\mathcal{B}} = \mathcal{M}_\theta(T'_t^{\mathcal{B}}, t^{\mathcal{B}})$
 - 9: Compute loss $\mathcal{L}(\theta; \mathbf{x}'_t^{\mathcal{B}}, \mathbf{q}'_t^{\mathcal{B}}, \mathbf{x}'_{\theta,1}^{\mathcal{B}}, \mathbf{q}'_{\theta,1}^{\mathcal{B}})$ Eq. 12
 - 10: Compute gradient $\nabla_\theta \mathcal{L}$
 - 11: Update parameters: $\theta \leftarrow \theta - \eta \nabla_\theta \mathcal{L}$
 - 12: **end for**
 - 13: **end for**
 - 14: **Return:** Trained model parameters θ^*
-

≤ 400 , we selected samples with scRMSD ≤ 2 ; for proteins with lengths ≥ 400 , we included samples with either scRMSD ≤ 2 or TM-score ≥ 0.9 . We also remove those with more than 50% loop and those with max 4% radius gyration. For the PDB dataset, we generated 20 proteins for each length in $\{60, 61, \dots, 512\}$, resulting in a reflow dataset containing 7,653 sample-noise pairs. For the SCOPe dataset, we generated 50 proteins for each length in $\{60, 61, \dots, 128\}$, producing a reflow dataset with 3,167 sample-noise pairs.

We set the batch size to 128 for an 80G GPU and use a learning rate of 0.0001. During inference, if exponential schedule is applied, the rate is set to 10.

B.5 Metrics

Designability. A protein backbone is considered designable if at least one amino acid sequence can fold into its structure. Our evaluation follows the methodology described in [35]. Specifically, for each generated backbone, we sample eight sequences using ProteinMPNN [6] with a temperature of 0.1. The folded structures of these sequences are then predicted using ESMFold [21], and their root mean square deviation (RMSD) is computed against the original backbone. A sample is classified as designable if its lowest RMSD—referred to as self-consistency RMSD (scRMSD)—is below 2 Å. The overall designability of a model is quantified as the fraction of samples that satisfy this condition.

Diversity. The measure of diversity we report follows the methodology from [2]. For each protein length specified above, we compute the average pairwise TM-score among designable samples, and then aggregate these averages across lengths. Since TM-scores range from zero to one, where higher scores indicate greater similarity, lower scores are preferable for this metric.

Novelty. We use foldseek [30] to calculate the max TM-score between the target protein and those in the database. We use the whole PDB dataset as our database, and the command is

```
foldseek easy-search <pdb_path> <database> <aln_file> <tmp_folder>
--alignment-type 1 \
--exhaustive-search \
```

Table 5: Unconditional protein backbone generation performance for 10 samples each length in $\{60, 61, \dots, 128\}$. We report the metrics from Section 4.1 and we indicate the best and top-3 results in the same way as Table 2 does.

	Efficiency		Designability		Diversity	Novelty	Sec. Struct.	
	Step	Time(s)	Fraction \uparrow	scRMSD \downarrow	TM \downarrow	TM \downarrow	Helix	Strand
Scope Dataset	-	-	-	-	-	-	0.330	0.260
FrameFlow	500	16.18	0.849	1.448 (± 1.114)	0.397	0.858 (± 0.059)	0.439	0.236
	400	13.43	0.864	1.353 (± 0.890)	0.380	0.859 (± 0.067)	0.452	0.229
	300	9.80	0.861	1.422 (± 1.178)	0.383	0.870 (± 0.062)	0.449	0.230
	200	6.61	0.842	1.496 (± 1.411)	0.378	0.854 (± 0.062)	0.437	0.237
	100	3.19	0.823	1.517 (± 1.228)	0.378	0.848 (± 0.061)	0.426	0.238
	50	1.69	0.820	1.546 (± 1.316)	0.379	0.836 (± 0.064)	0.441	0.228
	20	0.69	0.713	1.918 (± 1.495)	0.362	0.803 (± 0.071)	0.416	0.219
	10	0.35	0.504	2.924 (± 2.362)	0.344	0.782 (± 0.084)	0.363	0.213
ReFrameFlow	500	16.24	0.897	1.368 (± 1.412)	0.403	0.857 (± 0.052)	0.501	0.187
	400	13.29	0.893	1.328 (± 0.763)	0.402	0.858 (± 0.052)	0.489	0.202
	300	10.27	0.888	1.313 (± 0.686)	0.401	0.860 (± 0.047)	0.485	0.199
	200	6.60	0.907	1.326 (± 0.761)	0.403	0.852 (± 0.051)	0.482	0.206
	100	3.65	0.886	1.322 (± 0.804)	0.408	0.853 (± 0.057)	0.499	0.201
	50	1.65	0.903	1.291 (± 0.763)	0.400	0.850 (± 0.053)	0.504	0.202
	20	0.68	0.871	1.416 (± 0.880)	0.401	0.846 (± 0.050)	0.528	0.190
	10	0.33	0.806	1.696 (± 1.093)	0.390	0.814 (± 0.056)	0.496	0.192
QFlow	500	12.22	0.907	1.263 (± 1.334)	0.389	0.868 (± 0.057)	0.498	0.214
	400	10.11	0.907	1.199 (± 0.847)	0.390	0.873 (± 0.060)	0.476	0.223
	300	7.25	0.910	1.243 (± 1.027)	0.393	0.876 (± 0.056)	0.503	0.209
	200	4.78	0.877	1.309 (± 1.208)	0.389	0.864 (± 0.068)	0.481	0.224
	100	2.48	0.903	1.283 (± 1.027)	0.385	0.884 (± 0.052)	0.476	0.225
	50	1.33	0.872	1.389 (± 1.314)	0.371	0.863 (± 0.064)	0.491	0.206
	20	0.56	0.764	1.764 (± 1.529)	0.367	0.814 (± 0.071)	0.492	0.192
	10	0.29	0.565	2.589 (± 2.216)	0.348	0.772 (± 0.081)	0.467	0.167
ReQFlow	500	12.18	0.972	1.043 (± 0.416)	0.416	0.868 (± 0.046)	0.507	0.228
	400	10.01	0.962	1.050 (± 0.445)	0.416	0.864 (± 0.053)	0.523	0.212
	300	7.13	0.962	1.076 (± 0.518)	0.415	0.864 (± 0.050)	0.498	0.233
	200	4.80	0.948	1.084 (± 0.509)	0.406	0.862 (± 0.050)	0.513	0.218
	100	2.43	0.933	1.123 (± 0.669)	0.420	0.861 (± 0.053)	0.514	0.310
	50	1.27	0.932	1.162 (± 0.812)	0.415	0.855 (± 0.053)	0.491	0.237
	20	0.51	0.929	1.214 (± 0.633)	0.404	0.844 (± 0.053)	0.514	0.307
	10	0.26	0.848	1.546 (± 0.944)	0.403	0.827 (± 0.058)	0.518	0.195

```
--max-seqs 1000000000 \
--tmscore-threshold 0.0 \
--format-output query,target,alntmscore,lddt
```

where $\langle \text{pdb_path} \rangle$ is the path of the generated structure as a PDB file, $\langle \text{database} \rangle$ is the path to foldseek database, $\langle \text{aln_file} \rangle$ and $\langle \text{tmp_folder} \rangle$ specify the output file and directory for temporary files.

Efficiency To ensure fairness, we measure inference time on idle GPU and CPU systems. For PDB-based models, we sampled 50 proteins of length 300 and reported the mean sampling time.

Similarly, for SCOPe-based models, we sampled 50 proteins of length 128 and reported the mean sampling time. File saving and self-consistency calculations were excluded from the timing.

B.6 Baselines

Genie2 We use the code from Genie2 public repository. We loaded the base checkpoint trained for 40 epochs. The noise scale was set to 1 for full temperature sampling and 0.6 for low temperature sampling.

RFdiffusion We use the code from RFdiffusion public repository. Default configuration of the repository was used for sampling.

FoldFlow We use the code from FoldFlow public repository, which contains both FoldFlow and FoldFlow2. We set `noise_scale` to 0.1 and `flow_matcher.so3.inference_scaling` to 10 to achieve best performance.

FrameFlow We install FrameFlow from its public repository. Model weights are downloaded from here.

FrameDiff We used the code from FrameDiff public repository. The checkpoint we use is located in `./weights/paper_weights.pth`. We use the provided conda environment and default configuration for sampling.

C More Experimental Results

C.1 Detailed Comparisons Based on SCOPe

Table 5 presents comprehensive results from the SCOPe experiment, further demonstrating the superiority of the QFlow model and the reflow operation, especially in the context of ReQFlow. Notably, even with a generation process as concise as 10 steps, ReQFlow achieves a designable fraction of 0.848, while having an impressively fast inference time of just 0.26 seconds per protein. This highlights the efficiency and effectiveness of ReQFlow in generating feasible protein structures within a minimal timeframe. Additionally, both QFlow and ReQFlow models produce proteins with reasonable secondary structure distributions, indicating their capability to generate structurally plausible proteins. These findings underscore the potential of these models to significantly advance the field of protein design by balancing computational efficiency with structural accuracy.

C.2 Comparisons on Model Size and Training Data Size

The comparison of model size and training dataset size is listed in Table 6. Model sizes in the table refer to the number of *total* parameter. FoldFlow2 utilizes a pre-trained model, thus having 672M parameters in total. The number of trainable parameters is 21M.

C.3 Visualization Results

We use *Mol Viewer* [25] to visualize protein structures generated by different models, as shown in Figure 8 and Figure 9. In Figure 8, all proteins originate from the same noise initialization generated by QFlow, whereas in Figure 9, the initialization is generated by FoldFlow. Each method follows its own denoising trajectory, leading to distinct structural outputs. FoldFlow2 adopts a default sampling step of 50, while all other methods use 500 steps. Due to architectural differences, the final structures vary across models, but within the same model, different sampling steps generally yield

Table 6: Model Sizes and Training Dataset Sizes

Model	Training Dataset Size	Model Size (M)
RFDiffusion	>208K	59.8
Genie2	590K	15.7
FrameDiff	23K	16.7
FoldFlow(Base,OT,SFM)	23K	17.5
FoldFlow2	~160K	672
FrameFlow	23K	16.7
QFlow	23K	16.7
ReQFlow	23K+7K	16.7

¹ When training ReQFlow, we first apply the 23K samples of PDB to train QFlow, and then we use additional 7K samples generated by QFlow in the flow rectification phase.

Table 7: Comparisons for various methods on their performance (Fraction Score) in long backbone generation. The lengths of the generated backbones range from 300 to 600. We generate 50 samples for each length. We bold the best result and show the top-3 results with a blue background.

Length N	300	350	400	450	500	550	600
RFDiffusion	0.76	0.70	0.46	0.36	0.20	0.20	0.10
Genie2	0.86	0.90	0.74	0.58	0.28	0.12	0.10
FoldFlow2	0.96	0.88	0.70	0.56	0.60	0.26	0.16
FrameDiff	0.24	0.18	0.00	0.00	0.00	0.00	0.00
FoldFlow-OT	0.62	0.48	0.30	0.10	0.04	0.00	0.00
FrameFlow	0.78	0.76	0.54	0.38	0.30	0.12	0.02
QFlow	0.88	0.78	0.54	0.50	0.30	0.02	0.00
ReQFlow	0.98	0.98	0.86	0.80	0.92	0.68	0.34

similar structures. Notably, the noise distributions produced by QFlow and FoldFlow exhibit slight discrepancies, and models generally perform better on its own noise.

Among all models, ReQFlow exhibits the most stable and robust performance, maintaining low RMSD and variance across different sampling steps while demonstrating resilience to varying noise inputs. In contrast, other methods show significant limitations. Although FoldFlow2 achieves low RMSD at 50 and 100 steps, it lacks diversity and novelty, as reflected in Table 2. FoldFlow-OT is highly sensitive to initial noise, displaying drastically different performance in Figure 8 and Figure 9—evidenced by substantial variance across sampling steps when using QFlow noise. Moreover, FoldFlow-OT tends to overproduce α -helices—coiled, spiral-like structures—resulting in high designability scores but deviating from realistic protein distributions. Conversely, ReQFlow and QFlow generate a higher proportion of β -strands, which appear as extended, ribbon-like structures, indicating a closer alignment with natural protein distributions. This pattern suggests a high risk of mode collapse, where the model predominantly learns a specific subset of protein structures, leading to a lack of diversity and novelty. Furthermore, as sampling steps decrease, most baseline models experience a sharp deterioration in quality: RMSD values increase, rendering the structures non-designable. In extreme cases, some samples exhibit severe fragmentation or disconnected backbones (e.g., the dashed regions in FoldFlow2 at 20 steps, Figure 8), highlighting instabilities in their sampling dynamics.

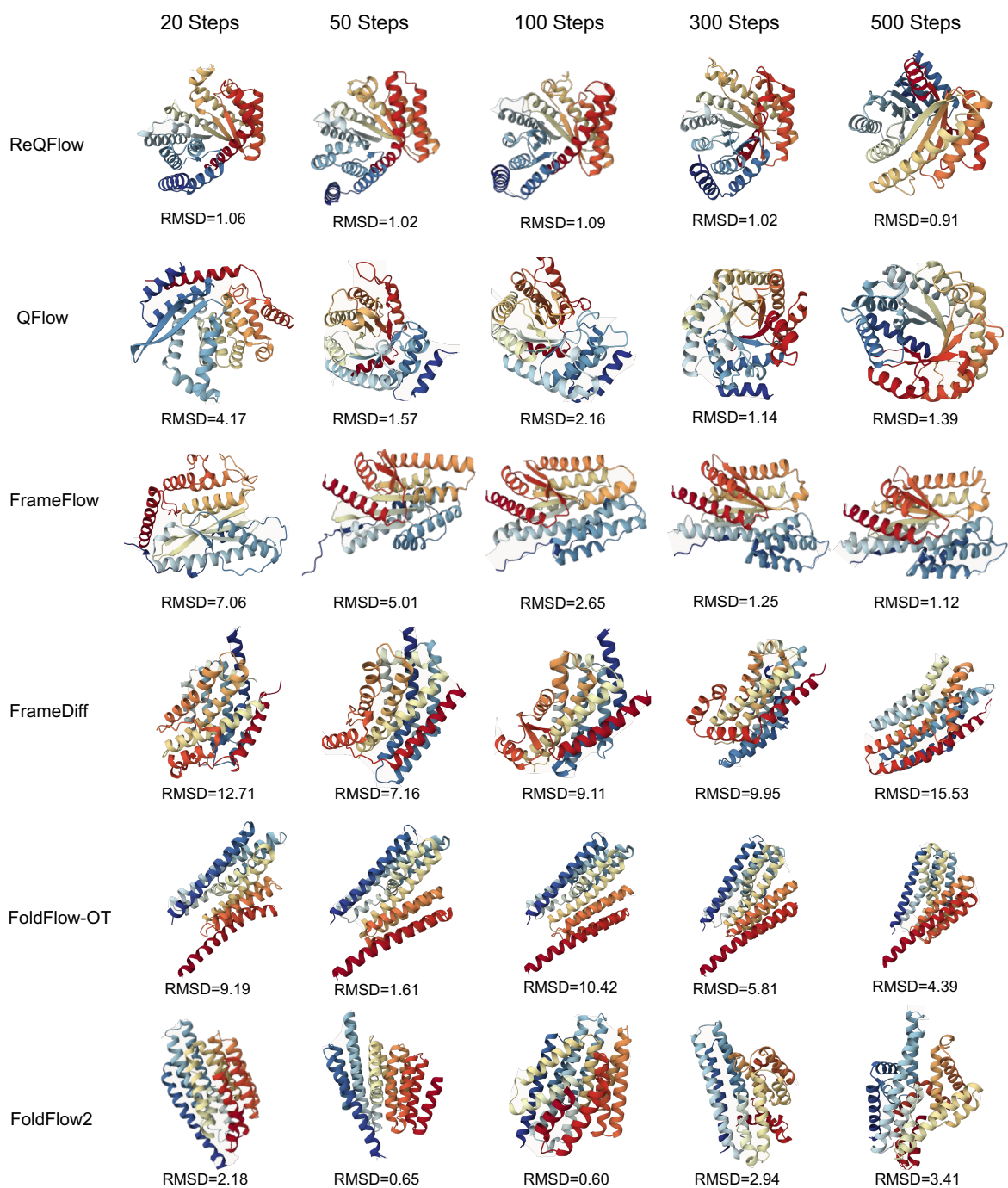


Figure 8: Visualization of different methods on length 300. Sampling start with a *same* noise generated by QFlow.

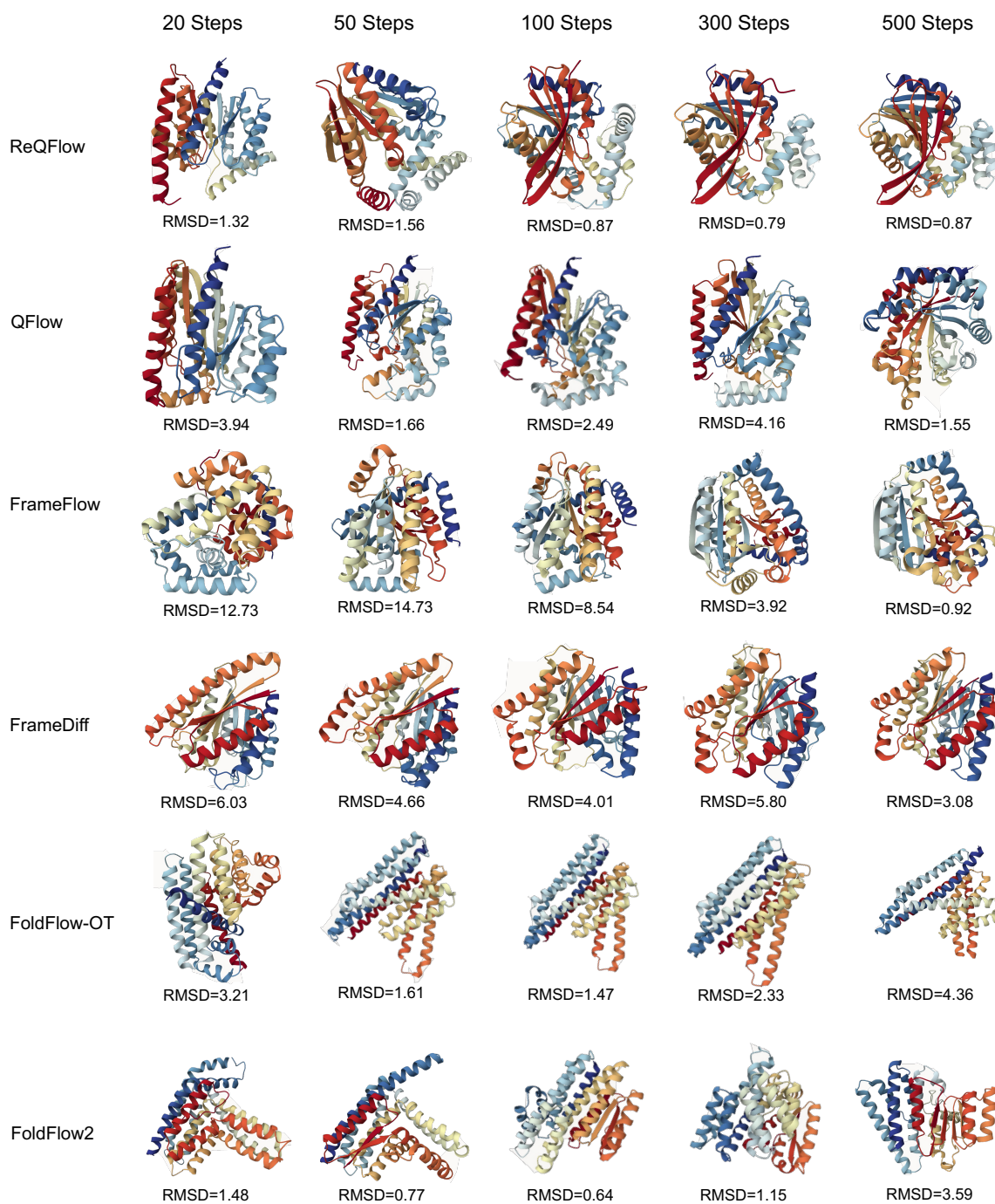


Figure 9: Visualization of different methods on length 300. Sampling start with a *same* noise generated by FoldFlow.